JOURNAL OF GEOPHYSICAL RESEARCH, VOL. 99, NO. B1, PAGES 711-728, JANUARY 10, 1994

Recent large earthquakes near Cape Mendocino and in the Gorda plate: Broadband source time functions, fault orientations, and rupture complexities

Aaron A. Velasco,[1] Charles J. Ammon, and Thorne Lay

Institute of Tectonics and C. F. Richter Seismological Laboratory, University of California, Santa Cruz

The northward migration of the Mendocino Triple Junction is associated with complex faulting within the Gorda plate and in the convergent zone between the Gorda and North American plates. This region has experienced substantial recent large earthquake activity, and quantification of these faulting processes is essential for understanding the evolution of the triple junction. Using an empirical Green function deconvolution method for teleseismic and regional surface waves and body waves, we obtain relative source time functions for the April 25, 1992, Cape Mendocino thrust earthquake (M_W = 7.2), its two large strike-slip aftershocks on April 26, 1992 (M_W = 6.5, 6.6), and two large strike-slip events in the Gorda plate that occurred July 13, 1991 (M_W = 6.8), and August 17, 1991 (M_W = 7.1). The removal of propagation effects using empirical Green functions provides unusually detailed source rupture information and indicates that all the ruptures are less than 16 s in duration. Analyzing the directivity effects observed in the source time functions, we resolve rupture directions and corresponding fault orientations for the four largest events and place some constraints on the smaller aftershock. Significant differences in the rupture duration and stress drop are observed between the Cape Mendocino mainshock and its two largest aftershocks. The mainshock, which ruptured westward on a shallow dipping plane either on or paralleling the interplate contact between the Gorda and North American plates, had a smooth 9-s-long rupture with a 0.9-4.6 MPa static stress drop. The two largest aftershocks occurred within the uppermost mantle of the Gorda plate and have more complex ruptures with total durations of 14-15 s and static stress drops of less than 0.3 MPa, perhaps reflecting a difference between mantle and crustal earthquakes in this region. The aftershocks appear to have ruptured conjugate strike-slip faults, accounting for differences in their damage patterns. The August 17, 1991, Gorda plate event ruptured a southwest striking fault, while the July 13, 1991, event ruptured a southeast striking fault, with both events relieving north-south compression within the deforming Gorda plate. The existence of multiple active faults in the region constitutes a significant earthquake hazard associated with the complex stress environment of the migrating triple junction.

Introduction

The Mendocino Triple Junction (MTJ) lies at the intersection of the Gorda, Pacific, and North American plates, in one of the most seismically active regions in the western United States. To the north, the Gorda plate subducts eastward beneath North America. To the south, the Pacific plate shears past the North American plate along the San Andreas Transform system; and to the west, the Mendocino fault forms the boundary between the Pacific and Gorda plates (Figure 1). Since July 1991 seven earthquakes with $M_W > 6$ have occurred within a few hundred kilometer distance from the MTJ (Table 1). In the following, we analyze the spatio-temporal faulting history of the largest five of these events.

The April 25, 1992, Cape Mendocino earthquake (M_W = 7.2) occurred in the immediate vicinity of the MTJ (Figure 1) and caused considerable damage to the towns of Ferndale, Fortuna, Petrolia, and Scotia, California [*National Earthquake Information Center (NEIC)*, 1992]. The focal mechanism of the Cape Mendocino event indicates predominantly thrust faulting [*Dziewonski et al.*, 1993b], but the event was followed on April 26, 1992, by two large strike-slip aftershocks located offshore in the upper mantle of the Gorda plate [*Dziewonski et al.*, 1993b; *NEIC*, 1992]. The occurrence of these earthquakes suggests significant coupling of the stresses between the Gorda and North American plates and highlights the complexity of fault interactions within the region. The first aftershock (M_W = 6.5; hereinafter referred to as AS 1) caused additional damage to the towns of Ferndale, Fortuna, Petrolia, and Scotia [*NEIC*, 1992]. The second, slightly larger aftershock (M_W = 6.6; hereinafter referred to as AS 2) contributed to damage within this region but, unlike the mainshock and AS 1, was also felt strongly in cities as far south as Santa Cruz and Salinas, California (~350-400 km) [*NEIC*, 1992]. Since AS 1 and AS 2 are virtually colocated and have similar focal mechanisms and seismic moments (Figure 1 and Table 1), the difference in seismic intensity patterns suggests that these earthquakes must involve different rupture directions, perhaps on conjugate planes. To understand the relationships between these events and the observed differences in seismic intensity, first-order information on the orientation of the fault planes and the time histories of faulting is required.

In 1991, two large strike-slip events occurred within the Gorda plate on July 13 (M_W = 6.8; hereinafter referred to as Gorda 1) and August 17 (M_W = 7.1; hereinafter referred to as

[1]Now at Lawrence Livermore National Laboratory, Livermore, California.

Paper number 93JB002390.
0148-0227/94/93JB-02390$05.00

Gorda 2). These are the largest intraplate events in the Gorda plate since the 1980 (M_W = 7.3) vertical strike-slip Eureka earthquake [*Smith et al.*, 1981; *Lay et al.*, 1982; *Turcotte et al.*, 1982]. Initial studies of aftershocks of these two events suggest that the earthquakes ruptured along northeast-southwest planes [*Gee et al.*, 1991], matching the orientation of mapped structures within the plate [*Silver*, 1971] as well as the fault-plane strike for the Eureka event. Unambiguously identifying the fault plane orientations for these events will help to decipher the nature of Gorda plate deformation.

Few seismological techniques can reliably distinguish between the fault plane and auxiliary plane of a focal mechanism. The most common method of identifying the fault plane orientation is by analysis of spatial trends in aftershock seismicity. However, even well-located aftershocks do not always present a simple pattern [e.g., *Ekström et al.*, 1992; *Stein and Ekström*, 1992], and using seismicity located on the periphery, or outside of a short-period network to identify the fault plane is usually difficult unless the event is very large. Geodetic measurements, which can also uniquely define the fault plane, suffer similar resolution problems when the event is relatively inaccessible or if a significant portion of the slip occurred offshore. In particular, identifying the Cape Mendocino mainshock rupture plane is complicated by the lack of thrust mechanism aftershocks [*Schwartz*, 1992], the fact that most aftershocks occurred offshore [*Oppenheimer et al.*, 1993] and by the complex interactions of faults in the immediate vicinity of the MTJ [*Jachens and Griscom*, 1983; *Furlong et al.*, 1989; D. Verdonck and G. Zandt, Three-dimensional crustal structure of the Mendocino Triple Junction region from earthquake travel times, submitted to *Journal of Geophysical Research*, 1993]. The Cape Mendocino aftershock patterns are diffuse and ambiguous with respect to defining the mainshock and large aftershock fault planes. The Gorda plate events occurred even farther offshore, outside the regional and local networks, resulting in poorly resolved mainshock and aftershock locations.

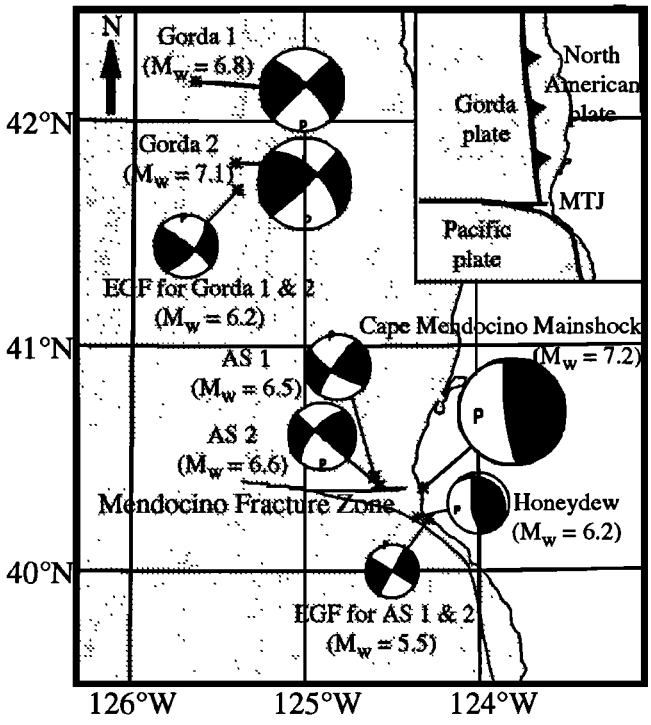

Fig. 1. NEIC epicentral locations and best double-couple focal mechanism solutions from the Harvard centroid-moment tensor (CMT) catalog for recent large earthquakes in the vicinity of the Mendocino Triple Junction (MTJ) and in the Gorda plate. Each event is labeled with its moment magnitude. The empirical Green function events chosen for each large event are also plotted. The inset shows the three plates that form the MTJ.

Earthquake fault planes can be determined from the seismic radiation if source radiation characteristics can be established for wavelengths and periods comparable to the spatio-temporal rupture extent. We extract source time functions from various phases using the empirical Green function deconvolution method adapted for teleseismic surface wave applications by *Ammon et al.* [1993] and A. A. Velasco, C. J. Ammon, and T. Lay, Empirical Green function deconvolution of broadband surface waves: Rupture directivity of the 1992 Landers, California (M_W = 7.3), earthquake, submitted to *Bulletin Seismological Soceity America* (1993). The essence of this technique is to deconvolve the mainshock recordings by signals from a nearby smaller earthquake with a similar faulting mechanism which intrinsically share common propagation and instrumental effects. For large events, rupture finiteness produces systematic patterns in the source time functions which allow fault plane identification through directivity analysis. The empirical Green function approach provides far

TABLE 1. National Earthquake Information Center and Centroid Moment Tensor Best Double Couple Earthquake Source Parameters

Event	Date	Time, UT	M_o,* N m	M_w,*	Latitude, deg	Longitude, deg	Depth,* km	Strike,* deg	Dip,* deg	Rake,* deg
Cape Mendocino (CM)	April 25, 1992	1806:04	6.69×10^{19}	7.2	40.37	-124.32	15	331	9	68
Honeydew (EGF for CM)	Aug. 17, 1991	1929:40	1.96×10^{18}	6.2	40.28	-124.25	10	311	22	51
Aftershock 1 (AS 1)	April 26, 1992	0741:40	5.96×10^{18}	6.5	40.42	-124.60	20	215	83	15
Aftershock 2 (AS 2)	April 26, 1992	1118:26	9.78×10^{18}	6.6	40.38	-124.57	22	132	89	157
EGF for AS 1 and 2	March 8, 1992	0343:04	1.85×10^{17}	5.5	40.23	-124.29	13	120	90	180
Gorda 1	July 13, 1991	0250:15	2.06×10^{19}	6.8	42.18	-125.64	11	315	78	-178
Gorda 2	Aug. 17, 1991	2217:15	4.43×10^{19}	7.1	41.82	-125.40	14	46	86	28
EGF for Gorda 1 and 2	Aug. 16, 1992	2226:17	3.13×10^{18}	6.2	41.70	-125.39	10	40	68	6

* From *Dziewonski et al.* [1992, 1993a,b].

more detailed source information than is normally retrieved from analysis of surface waves and enables a unified treatment of the source information extracted from both body and surface waves. This method has been used previously to determine the fault plane and slip functions for large events such as the 1992 Landers, California, earthquake (M_W = 7.3) [*Ammon et al.*, 1993; A. A. Velasco, C. J. Ammon, and T. Lay, submitted manuscript, 1993] and a preliminary analysis of the 1992 Cape Mendocino earthquake [*Ammon et al.*, 1993].

We examine the ruptures of the Cape Mendocino mainshock, expanding the data set analyzed by *Ammon et al.* [1993], the two 1991 Gorda plate events, and the two largest aftershocks of the Cape Mendocino earthquake. For four of the events we can confidently identify the fault plane from the observed azimuthal variation in source time history, with the fault plane for the smallest event being resolved with less confidence. To investigate the rupture complexity and to estimate the static stress drop of each event, we also analyze azimuthally averaged time histories which reflect the overall source characteristics. We then relate the finite source characteristics to the tectonic processes associated with this suite of events. The successful identification of the fault planes and rupture characteristics for offshore events of moderate size holds much promise for quantification of faulting in other complex regions.

TECTONIC BACKGROUND

The strike-slip/strike-slip/trench MTJ is an unstable triple junction [*Dickinson and Snyder*, 1979] that has migrated northward over the last 30 m.y. since the Pacific and North American plates first came into contact [*Atwater*, 1970]. The northward migration of the MTJ is responsible for the growth of the San Andreas fault system, which has evolved in its wake [*Atwater*, 1970]. On several occasions in the past, the MTJ appears to have jumped eastward [*Griscom and Jachens*, 1989; *Smith et al.*, 1993]. The Mendocino fault is seismically active with small-to-moderate size earthquakes, most of which are presumably right-lateral strike slip on east-west vertical fault planes [*Bolt et al.*, 1968; *Simila*, 1980; *Sverdrup*, 1987; *Smith et al.*, 1993]. North of the MTJ, the Gorda plate underthrusts beneath the North American plate along the Cascadia subduction zone, but there has been a marked absence of any historic interplate thrusting events, and the interplate boundary is not clearly illuminated by seismicity [*Smith et al.*, 1993]. The seismic hazard of the Cascadia subduction zone remains controversial, since no large thrust earthquakes have been recorded along it. However, mounting evidence exists for large prehistoric seismic events along the Pacific northwest [e.g., *Heaton and Kanamori*, 1984; *Heaton and Hartzell*, 1987; *Atwater*, 1987; *Spence*, 1989; *Muhs et al.*, 1990; *Savage and Lisowski*, 1991; *Clarke and Carver*, 1992]. In this context, the April 25, 1992, Cape Mendocino event takes on particular significance, especially with regard to confidently identifying the fault plane.

The accessibility of the MTJ has resulted in a number of tectonic studies and models of the plate interactions in this region [*Wilson*, 1986, 1989; *Griscom and Jachens*, 1989], investigations of coastal geology [*Kelsey and Carver*, 1988; *McCroy*, 1989; *Muhs et al.*, 1990], gravity modeling [*Griscom and Jachens*, 1989], shallow reflection profiling [*Silver*, 1971], imaging of *P* velocity variations (D. Verdonck and G. Zandt, submitted manuscript, 1993), and seismicity distribution [*Bolt et al.*, 1968; *Simila et al.*, 1975; *Cockerham*, 1984; *Smith et al.*, 1993]. Of particular interest has been characterizing the internal deformation of the Gorda plate. The Gorda plate deformation has been studied using seafloor magnetic anomalies [e.g., *Riddihough*, 1984; *Stoddard*, 1987] and has had many large intraplate earthquakes [*Bolt et al.*, 1968; *Turcotte et al.*, 1982; *Ellsworth*, 1990; *Stoddard and Woods*, 1990; *Dengler et al.*, 1992b]. These are generally attributed to internal deformation of the young oceanic lithosphere caused by north-south compression across the Mendocino fault.

EMPIRICAL GREEN FUNCTION DECONVOLUTION METHOD

Studies of earthquake processes by far-field seismic waveform modeling essentially involve determination of source time functions associated with particular observing positions (i.e., azimuths and ray parameters with respect to the source) [e.g., *Ruff and Kanamori*, 1983; *Ruff*, 1987]. Observed signals are complicated by the distinct propagation effects that obscure the radiation history at the source. For teleseismic body waves, simple velocity models are often sufficient to account for primary propagation effects, but such body waves provide very limited ray parameter coverage, reducing their sensitivity to source finiteness. Surface waves intrinsically provide superior sensitivity to horizontal rupture extent, but existing earth models are only adequate to account for propagation effects for long periods, greater than about 100 s. Thus surface wave inversions typically provide only point source information for events smaller than magnitude 7.5 [e.g., *Velasco et al.*, 1992]. To better exploit the surface wave information and to merge it in a self-consistent fashion with body wave information, we must forego use of current, inadequate propagation models.

To extract a high-resolution source time function of a large event from a particular arrival (an isolated body wave or a surface wavetrain), we use the corresponding recording of a nearby, much smaller event to remove the propagation effects from the signal of the larger event. The small event is referred to as an empirical Green function (EGF) and ideally should have a focal mechanism identical to that of the larger event [*Hartzell*, 1978; *Mueller*, 1985; *Hough et al.*, 1991; *Nakanishi*, 1991]. Widely distributed surface and body waveforms from the large event are deconvolved by the EGF recordings to isolate the source time functions of the large event for different azimuths and ray parameters [*Ammon et al.*, 1993; A. A. Velasco, C. J. Ammon, and T. Lay, 1993]. We perform the deconvolutions in the frequency domain using the water level method [*Helmberger and Wiggins*, 1971; *Clayton and Wiggins*, 1976]. The resulting time series are known as relative source time functions (RSTFs).

For moderate-sized events (M_W ~ 7.0 or smaller), to obtain a reliable RSTF for periods longer than a few seconds, the EGF must be located within about 1.5 fault lengths of the larger source and should be approximately an order of magnitude smaller than the larger event (A. A. Velasco, C. J. Ammon, and T. Lay, 1993). Below the EGF corner frequency, the waveforms from the EGF approximate the propagation impulse response for the given fault mechanism. If the EGF has a short, impulsive source duration (i.e., a relatively high corner frequency), the RSTFs are close approximations to the moment-normalized source time functions of the large event. For EGFs that are similar in size and rupture duration to the

larger event, gross characteristics of the rupture may be estimated, but high-frequency information about the rupture is irretrievable due to the low corner frequency of the EGF (C. J. Ammon, T. Lay, A. A. Velasco., and J. E. Vidale, Routine estimation of rupture complexity: The October 18, 1992, Colombian earthquake, submitted to *Bulletin Seismological Society America*, 1993).

The usable bandwidth for the time function analysis depends on the size of the EGF, the distance between the EGF and the larger event, and the intrinsic signal-to-noise characteristics of the wave type (*P*, *SH*, surface wave). We low-pass filter the RSTFs to eliminate high-frequency noise and frequencies inappropriate for the available EGF. The high-frequency corner of the filter depends primarily on the EGF corner frequency and, for surface waves, on dispersion effects caused by differences in location between the EGF and mainshock. To estimate rupture characteristics of an earthquake, the observable periods of the RSTFs must be smaller than the rupture duration. The low-frequency end is commonly limited by signal-to-noise ratio for the EGF, and occasionally band-pass filtering is necessary.

Directivity Determination

To determine rupture direction and estimate subevent centroid locations, the relative locations of discrete features in the RSTFs, such as the onsets, peaks, or terminations of moment release are estimated. In picking the times of RSTF features, we strive for consistency from trace to trace. Filter sidelobes and deconvolution noise make time picks of the onsets and ends of the RSTFs less reliable than measurements of peaks in the RSTFs. All absolute times are influenenced by the choice of source locations for the mainshock and EGF, and it is possible to locate mainshock features with respect to one another (e.g., onset to peak), or with respect to the EGF location (e.g., EGF to onset). The relative locations are estimated by directivity analysis [*Hirasawa*, 1965; *Schwartz and Ruff*, 1985; *Ammon et al.*, 1993; A. A. Velasco, C. J. Ammon, and T. Lay, 1993] based on the linear relationship, $\delta t = t_O - \Gamma\Delta$, where δt is the measured time difference between the chosen features (e.g., onset to peak; onset to end; onset to EGF location; peak to peak for two subevents), t_O is the true time delay between the features, and Δ is the horizontal distance between the two features. The directivity parameter Γ is defined as $\Gamma = \cos(\theta)/c$, where θ is the azimuth of the station relative to the azimuth of a line connecting the spatial offset between the features and c is the wave phase velocity. Each azimuth is investigated systematically to estimate Δ and t_O. The preferred azimuth corresponds to the rupture direction producing the best linear correlation coefficient. The fault plane can be identified by comparing the rupture azimuth estimated from features in the RSTFs and the two planes of the earthquake focal mechanism. Figure 2 illustrates expected directivity effects for a fault plane with geometry similar to the Cape Mendocino mainshock.

For a unilaterally propagating rupture, the total duration of time function at a station is given by

$$d = L\left(\frac{1}{v_r} - \frac{\cos\theta}{c}\right),$$

where d is the total duration, v_r is the rupture velocity, and L is the fault length. Thus the intrinsic sensitivity of each RSTF to source rupture directivity (i.e., the amount of azimuthal variation in time shift between features in the RSTFs) depends on both the rupture velocity and the phase velocity of the wave associated with that time function. Surface wave RSTFs are very sensitive to directivity since the rupture and phase velocities are comparable. However, surface waves are dispersive, and any wave train involves a range in phase velocities. A. A. Velasco, C. J. Ammon, and T. Lay (1993) addressed the issue of using surface wave deconvolutions in directivity analysis, and found that using the average Airy phase velocity value for c yields reasonable recovery of source finiteness for low-pass-filtered RSTFs.

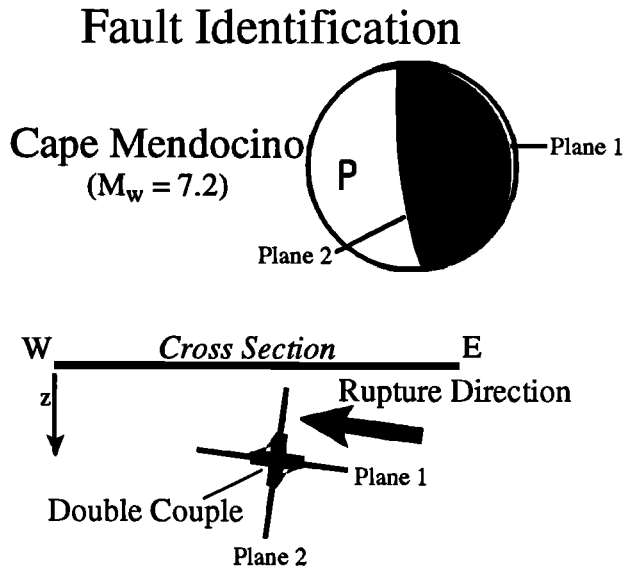

Fig. 2. Cartoon illustrating how the fault plane can be distinguished from the auxiliary plane using rupture directivity. For earthquakes with unilateral rupture, comparing the rupture direction inferred from far-field source time functions with the focal mechanism allows identification of the fault plane. This example corresponds to the Cape Mendocino mainshock. Detection of a unilateral component of westward rupture indicates that the shallow dipping plane 1 is the fault plane rather than the steeply dipping plane 2.

Data

We use digital recordings from globally distributed, broadband seismic stations operated by various networks, including the Incorporated Research Institutions for Seismology Global Seismic Network, the California Institute of Technology TERRAscope network, and the Berkeley Digital Seismic Network. We window the short-arc Rayleigh (R1) and Love (G1) waves from the seismograms using group velocity windows adjusted to ensure that the significant fundamental mode energy is completely included [*Ammon et al.*, 1993, A. A. Velasco, C. J. Ammon, and T. Lay, 1993]. Body waves (*P* and *SH*) are windowed individually. The phase of each deconvolution is sensitive to the origin times and epicentral locations used for both events, since the group-velocity window of each seismogram is referenced to these parameters. We use the NEIC values listed in Table 1 for these parameters. Small errors in the initial relative locations of the EGF and mainshock will be largely accounted for in the relative times of the RSTFs, although minor distortions of surface wave RSTFs can result.

Sensitivity of Deconvolutions to Source Depth Differences

Previous investigations have established guidelines for EGF selection associated with event size and distance from the

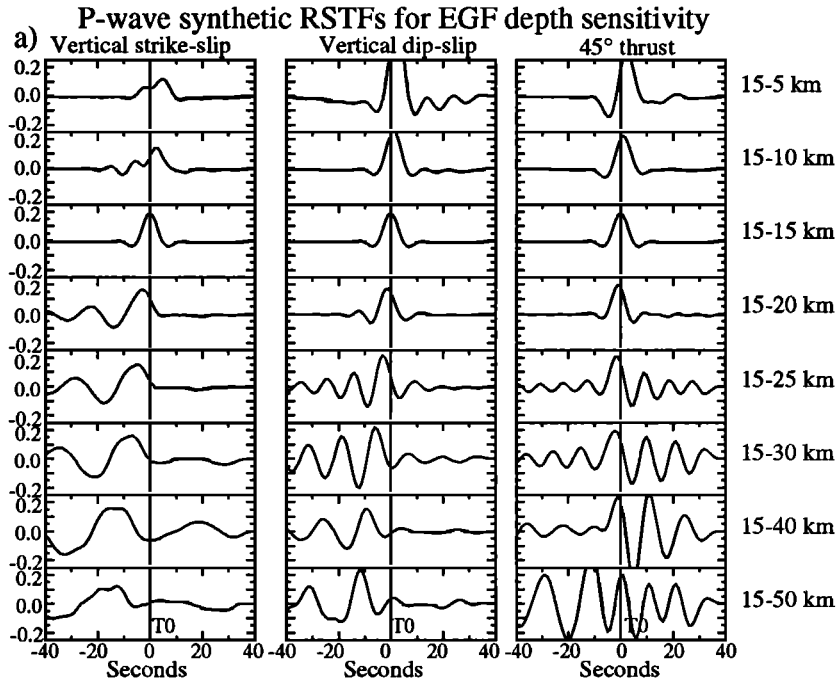

Fig. 3. (a) EGF depth sensitivity test for synthetic P wave deconvolutions for vertical strike-slip (left column), vertical dip slip (middle column), and 45° thrust (right column) focal mechanisms. (b) Sensitivity test for synthetic transverse component S wave deconvolutions for vertical strike slip (left column), vertical dip slip (right column). Each row shows deconvolutions of master event synthetics for a source at 15 km depth with synthetic Green functions at 5, 10, 15, 20, 25, 30, 40, and 50 km, as labeled on the right. No noise is added to the synthetics. The RSTFs have been low-pass filtered at 10 s. The row labeled 15-15 km is the exact deconvolution, with the RSTF corresponding to a low-pass-filtered delta function. The deconvolutions become unstable for depth differences greater than 20 km for P waves and 10 km for S waves, and biases in timing and pulse width appear for EGF/mainshock depth differences of more than 10 km.

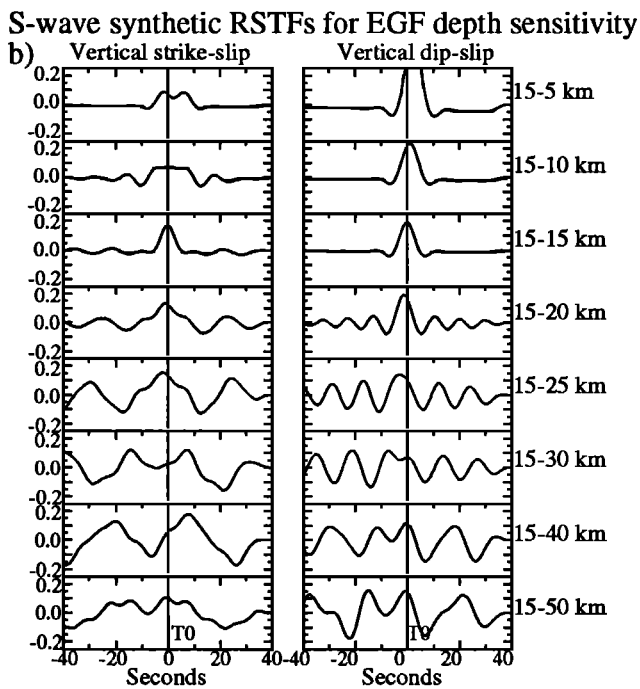

Fig. 3. (continued)

larger source (A. A. Velasco, C. J. Ammon, and T. Lay, 1993), but the influence of relative EGF depth has not been thoroughly documented. This is of particular relevance in this study because several of the events of interest are relatively small, placing greater demands on adequacy of the EGFs. Many studies have deconvolved Green functions computed for simple earth structures from body wave seismograms to obtain source time histories and/or focal mechanisms [e.g., *Kikuchi and Kanamori*, 1982, 1986, 1991; *Ruff and Kanamori*, 1983; *Ruff*, 1987]. Since P waveforms are sensitive to the interference of depth phases (pP, sP), differences in depth between an earthquake and the Green function can significantly affect deconvolved RSTFs [*Christensen and Ruff*, 1985]. *Christensen and Ruff* [1985] showed that depth differences of 20 km can significantly distort the estimated source time functions. We use synthetic seismograms in our procedure to investigate the effect of EGF depth differences on the body wave and surface wave deconvolutions.

We compute P wave synthetics for the three fundamental dislocations, vertical strike-slip, vertical dip-slip, and 45° thrust focal mechanisms, and transverse component S wave synthetics for vertical strike-slip and vertical dip-slip mechanisms. We set the depth of our reference event to be 15 km and deconvolve calculated Green functions computed at depths of 5, 10, 15, 20, 25, 30, 40, and 50 km (Figure 3a and 3b). The epicentral distance used in the calculations is not very important when no noise is included since there is not much loss of bandwidth, however, for data this can be a factor. The deconvolutions are low-pass filtered at 10 s. Ten kilometer depth differences begin to affect amplitudes of the P wave deconvolutions (Figure 3a), but durations of the time functions can be recovered with only slight bias. For each focal mechanism type, the deconvolutions for P waves become unstable for depth differences of 20 km or larger, consistent with the results of *Christensen and Ruff* [1985]. S wave deconvolutions are more sensitive to depth differences than P wave deconvolutions, with 10 km depth differences significantly affecting the results (Figure 3b). In order to obtain reliable durations from the body wave deconvolutions,

the EGF source depth must be within 10-15 km of the centroid depth of the larger event.

We now test the effect of depth difference between an EGF and a larger event for surface wave deconvolutions. Synthetic seismograms are calculated for an isotropic, plane-layered velocity model approximating preliminary reference Earth model (PREM) [*Dziewonski and Anderson*, 1981] with a 20-km-thick crust. The calculations were performed using the method and programs of *Herrmann* [1987] and are appropriate for plane-layered Earth models. We deconvolve Rayleigh and Love wave Green functions computed for depths of 5, 10, 15, 20, 25, 30, 40, and 50 km from a 15-km-deep reference event for vertical strike-slip, vertical dip-slip, and 45° thrust focal mechanisms (at an azimuth of 30°) (Figure 4). The deconvolutions are low-pass filtered at 10 s. For vertical dip-slip and 45° thrust earthquakes, the pulse widths of Rayleigh wave RSTFs can be recovered with up to 20 km depth differences, and the amplitudes are affected by a factor of less than 1.5 (Figure 4a). For a vertical strike-slip earthquake, the EGF must be within 10 km depth difference to reliably obtain

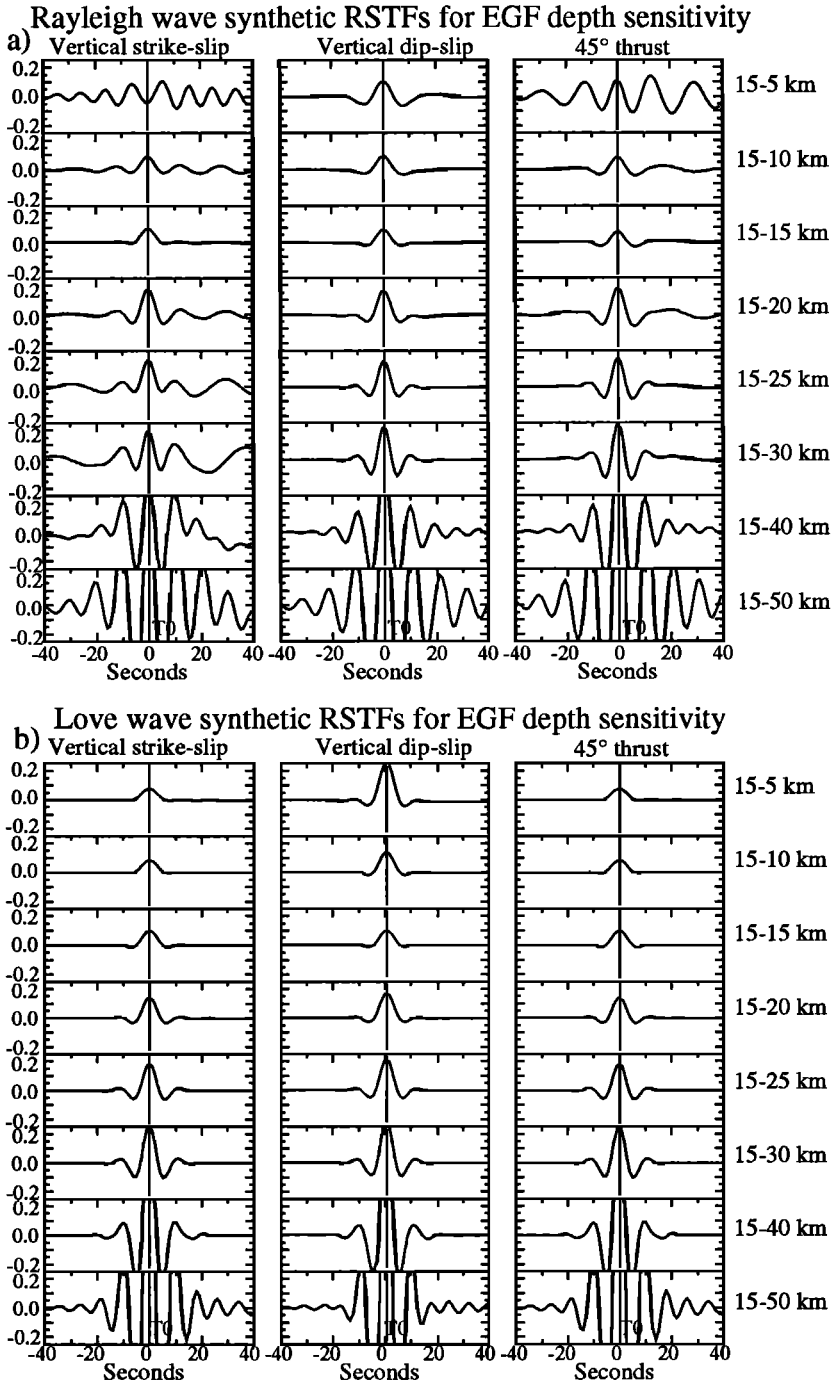

Fig. 4. EGF depth sensitivity test for synthetic (a) Rayleigh and (b) Love wave deconvolutions calculated for vertical strike-slip, vertical dip-slip, and 45° thrust focal mechanisms. Each row shows deconvolutions of master event synthetics for a source at 10 km depth with synthetic Green functions at 5, 10, 15, 20, 25, 30, 40, and 50 km, as labeled on the right. The RSTFs have been low-pass filtered at 10 s. The second row is the exact deconvolution, showing the impulse response of the filter. Rayleigh waves are more sensitive to depth differences than Love waves.

both duration and amplitude (Figure 4a). Love waves are much less sensitive to depth differences, and the pulse width can be reliably obtained with up to 20-25 km depth differences (Figure 4b). However, amplitudes are significantly affected for depths differences larger that 15 km. We include body waves and surface waves in the following analyses, and for all EGF-mainshock pairs, EGF depths are within 10 km of their mainshocks (Table 1).

RELATIVE SOURCE TIME FUNCTIONS, DIRECTIVITY, AND FAULT PLANE ORIENTATIONS

The larger earthquakes (M_W > 6.5) that have occurred in the past 2 years near Cape Mendocino and in the southern Gorda plate all have suitable EGFs (Table 1). Gorda 2 was preceded by a moderate-sized event on August 16, 1991 (M_W = 6.2), located very close to the mainshock epicenter with a similar focal mechanism. We use the latter event as an EGF for both Gorda 1 and Gorda 2. Approximately 3 hours preceding Gorda 2, the August 17, 1991, Honeydew earthquake (M_W = 6.2) occurred about 200 km to the southeast, very near the future epicenter of the April 25, 1992, Cape Mendocino earthquake. The Honeydew event appears to be a preshock to the Cape Mendocino earthquake since its location and mechanism are very similar to the mainshock. We use this earthquake as an EGF for the Cape Mendocino mainshock. We were unable to identify a suitable EGF for the Honeydew earthquake itself, due to the paucity of thrust events in the region. Several candidate EGFs for the Cape Mendocino aftershocks were examined before we chose a strike-slip event that occurred March 8, 1992 (M_W = 5.5), near the epicenter of the Honeydew earthquake. This event is farther from the aftershocks than is optimal, but it was well recorded on regional and teleseismic stations, providing necessary azimuthal coverage. Unfortunately, there is no more than one high-quality EGF available for each mainshock, so at present we are unable to thoroughly explore sensitivity to EGF selection. Future earthquake activity will allow an analysis of the sensitivity of our results to the EGF.

April 25, 1992, Cape Mendocino, California, Earthquake

We deconvolved more than 50 distinct phases of the Honeydew event from the Cape Mendocino event and achieved uniform sampling of the directivity function in the range -0.25 to +0.25 s/km (using teleseismic *P* waves alone only provides coverage from about -0.05 to +0.05 s/km). We low-pass filter the RSTFs at 5 s since an initial estimate of the rupture duration is about 10 s [*Ammon et al.*, 1993]. We compared 5- and 10-s low-pass filters of the RSTFs and found that a low-pass filter at 5 s can be used due to the close proximity of the two events and given that the corner frequency of the Honeydew event is greater than 0.2 Hz. The 5-s filtered body and surface wave RSTFs do not indicate significant rupture complexity (Figure 5), but there is some azimuthal variation in pulse width. We use these RSTFs to estimate variations in risetime and pulse width and perform a directivity analysis using the onset, peak, and end time picks.

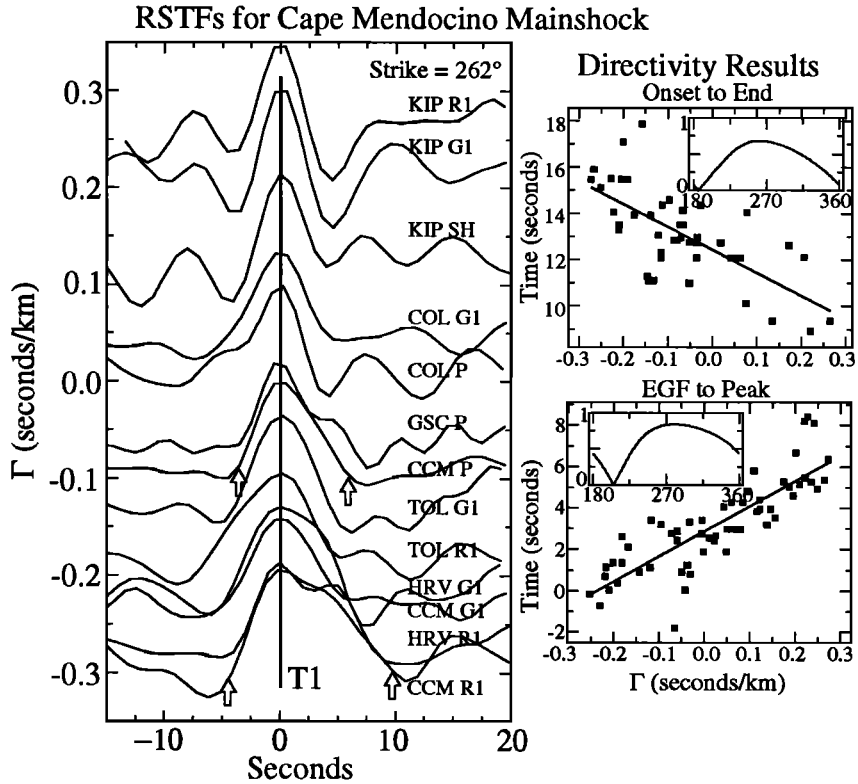

Fig. 5. (left) Deconvolved RSTFs of the Cape Mendocino earthquake plotted as a function of the directivity parameter Γ referenced to the optimal rupture azimuth of 262°. The functions have been low-pass filtered at 5 s. Each RSTF is labeled with the station name and phase, and all RSTFs are aligned by their peak times, T1. Open arrows demonstrate time picks for *P* and Rayleigh wave phases at station CCM. Note the shorter durations near Γ = 0.2 s/km and longer durations near Γ = -0.2 s/km. (right) Directivity analysis for the onset to end (right top) and EGF to peak (right bottom) time picks. The inset shows the variation of the linear correlation coefficient as a function of azimuth. Squares correspond to observations, the best fitting line is indicated by the solid line, with the plots being for the rupture azimuth with the maximum correlation coefficient.

To minimize the bias in our time picks, we locate the onset, peak, and end of the RSTFs relative to the EGF as well as locating the peak and end of the source time function relative to the onset. In Figure 5 we present the RSTFs as a function of the directivity parameter (Γ) for the preferred rupture direction (262°), along with the directivity analysis results for the onset to end and EGF to peak time picks. Ordering the RSTFs as a function of the directivity parameter illustrates the systematic pulse width variations caused by the unilateral component of directivity. RSTF pulse widths narrow as the rupture propagates toward stations with larger positive Γ. For stations with larger negative Γ, RSTFs become longer in duration, since the rupture propagates away.

Care must be taken when using onset and end time picks for directivity analysis, since bias in these times exists due to the effects of the low-pass filter. Furthermore, some RSTFs at distant stations in the Chinese Digital Seismic Network (CDSN) such as BJI, KMI, and LZH lack higher frequencies relative to other stations. The spectral falloff occurs around 20 s for all the signals at these stations, biasing the onset to end time picks in the deconvolved traces. Even though the EGF deconvolution should correct for any instrument effects, we find that the longer periods dominate at these stations, resulting in anomalously long-duration estimates for the onset to end time picks. Possibly, propagation along these paths severely attenuates the higher frequencies. Equally possible is that these stations do not record high frequencies above the noise level for the EGF due to the relatively narrow-band CDSN instrument response. Other instruments at distances greater than 60°, such as TOL, do not show this biased broadening. Thus, for moderate-sized and smaller events with rupture durations less that 15 s, caution must be taken when analyzing the RSTFs, since intrinsic bandwidth of the recording instruments may influence estimates of duration. These filtering effects will always lead to underestimation of the rupture velocity.

The Cape Mendocino rupture propagated west-southwest at an azimuth of 262 ± 26° with a maximum duration of 12.4 ± 0.2 s (Table 2). This statement applies to that part of the rupture associated with a unilateral component, and the directivity procedure may fail to detect any bilateral or radially expanding rupture component. We observe about 5 s of azimuthal variation in duration, with 3-4 s of scatter at each directivity parameter, but the data define a very consistent trend. The rupture velocity inferred from the propagation distances and relative times are small, less than 1 km/s, but this may reflect overestimation of the relative times due to the filter sidelobes, bandwidth limitations, and deviations from simple unilateral rupture. In practice, it is difficult to correct for filter sidelobes due to complex interference with noise and slight inadequacies of the EGF. We will show later that stacking the time functions to improve the signal-to-noise level reduces the total duration estimate by about 3 s, with even that being an upper bound due to the broadening effect of finite bandwidth.

The peak of the moment release relative to the Honeydew event (EGF to peak) locates just onshore, with a high correlation coefficient (0.84) (Figure 5 and Table 2). Given the symmetric shape of the RSTFs, the peak of the RSTFs roughly corresponds to the centroid of the moment release. Locations of the onset, peak, and end relative to the EGF support the model of a west-southwest directed rupture with a large portion of moment release occurring just onshore (Table 2), but the estimates of onset and end locations relative to the EGF are likely to be biased by the filtering. Geodetic modeling gives a maximum displacement vector that coincides with our rupture direction, with the maximum displacements occurring at the coast [*Oppenheimer et al.*, 1993]. However, the geodetic model accounts for only 60% of the seismic moment, suggesting that more moment may be released off-shore, as indicated in our model. The rupture direction is consistent with thrusting motion on the shallow, east-northeasterly dipping fault.

TABLE 2. Directivity Analysis

Event Pair (From / to)	Time Separation, s	Correlation Coefficient	Distance, km	Azimuth, deg
		Cape Mendocino Mainshock		
EGF to Onset	-3.9±0.2	0.81	13.4±1.3	291±36
EGF to Peak	2.9±0.2	0.84	12.2±1.1	280±32
EGF to End	9.8±0.3	0.66	13.8±2.1	265±29
Onset to Peak	6.1±0.2	0.54	4.2±1.0	267±26
Onset to End	12.4±0.2	0.69	9.9±1.6	262±26
		Aftershock 1 (Small)		
EGF to Onset	-4.4±0.8	0.87	28.6±4.1	333±58
EGF to Peak	5.5±0.5	0.94	32.8±3.1	356±47
EGF to End	12.2±0.7	0.88	26.5±3.7	354±42
Onset to Peak	9.9±1.3	0.33	12.8±9.3	56±34
Onset to End	17.0±1.3	0.32	10.0±7.8	87±27
		Aftershock 2 (Large)		
EGF to Onset	-6.9±0.9	0.79	31.3±5.5	305±34
EGF to Peak1	-2.5±0.9	0.75	28.3±5.6	299±33
EGF to Peak2	2.3±0.8	0.71	21.5±5.6	284±29
EGF to End	6.9±0.8	0.60	16.5±5.1	285±30
Peak 1 to Peak 2	5.8±0.6	0.72	11.8±3.4	148±34
Onset to Peak1	4.4±0.6	0.22	4.4±4.4	168±33
Onset to Peak2	9.2±0.9	0.47	13.7±5.8	160±34
Onset to End	13.5±0.9	0.52	15.1±5.5	143±35
		Gorda Plate 1 (Mw = 6.8)		
EGF to Onset	-4.1±0.6	0.89	48.5±4.2	2±22
EGF to Peak1	1.0±0.5	0.91	45.1±3.6	1±22
EGF to Peak2	4.5±0.6	0.87	43.5±4.2	12±22
EGF to End	8.7±0.5	0.88	41.2±3.8	10±21
Peak 1 to Peak 2	4.3±0.6	0.60	11.4±3.5	120±32
Onset to Peak1	4.7±0.2	0.26	1.9±1.5	112±31
Onset to Peak2	8.7±0.5	0.42	7.7±2.8	123±30
Onset to End	12.9±0.5	0.40	7.8±3.1	143±31
		Gorda Plate 2 (Mw = 7.1)		
EGF to Onset	-4.1±0.2	0.77	8.4±1.3	316±24
EGF to Peak	-0.7±0.2	0.88	9.1±1.0	304±24
EGF to End	2.8±0.2	0.76	8.5±1.4	296±25
Onset to Peak	3.3±0.1	0.46	1.5±0.6	204±26
Onset to End	6.8±0.2	0.45	2.9±1.1	217±24

Our inferred locations of the Cape Mendocino rupture onset and centroid are west of the epicentral location from CALNET (Figure 6). While we have little confidence in our ability to locate the onset, due to the filter sidelobes and bandwidth limitations, we are confident that the centroid of the rupture is west to northwest of the Honeydew event, in contrast to the epicentral locations given by CALNET. One possible explanation for the discrepancy is the occurrence of a small precursory energy release at the onset of the mainshock located east of the major moment release. At station COR (Δ = 4.3°; Az = 8.8°), a small precursor to the Cape Mendocino mainshock appears on the vertical component which is not evident for the Honeydew earthquake (Figure 7). The fact that the Honeydew seismogram at COR does not show this precursor suggests that it is not a structural arrival, but the noise level of the Honeydew recording may be too high to detect any precursory structural arrival. We do not observe this precursor at other close

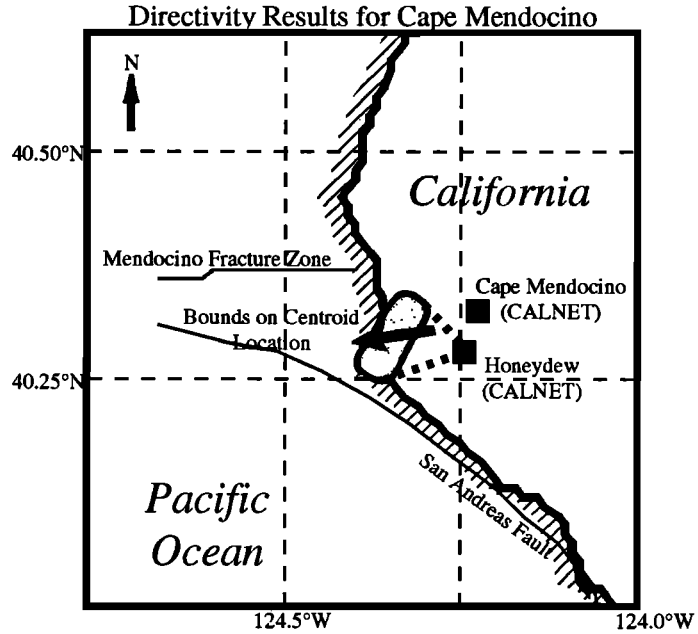

Fig. 6. The Cape Mendocino mainshock centroid location (shaded region) obtained from directivity analysis. The shaded region encompasses one standard deviation from the centroid location derived from the directivity analysis. The solid arrow shows only the rupture direction. The rupture propagated westward, and a significant part of the moment release was just onshore. The CALNET locations of the onset of rupture for the mainshock and the Honeydew event are also shown.

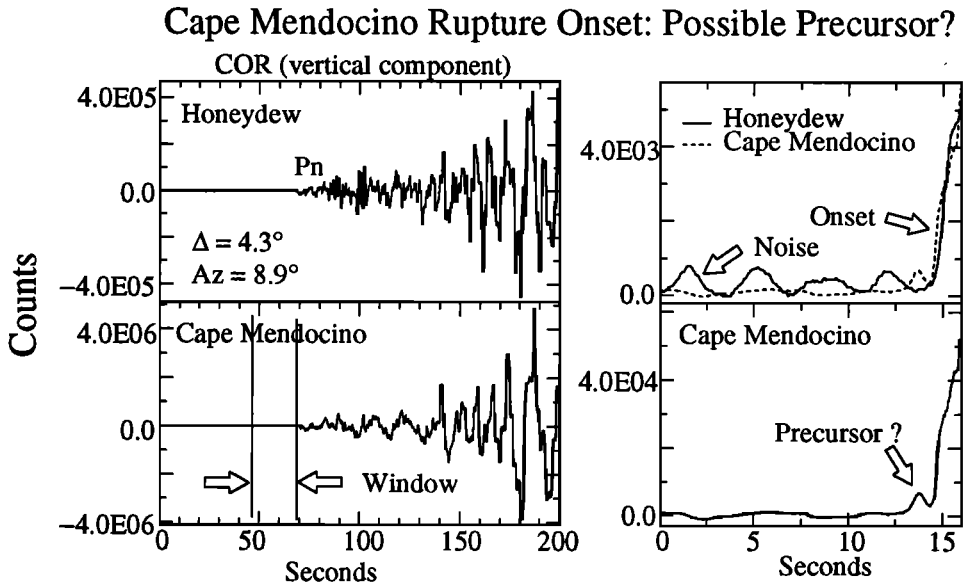

Fig. 7. The broadband vertical component (proportional to velocity) at station COR (Corvallis, Oregon; Δ = 4.3°; Az = 8.9°) shows evidence of a small precursor to the Cape Mendocino mainshock that is not found for the Honeydew earthquake.

stations such as CMB (Δ = 3.8°; Az = 126°); however, the overall complexity of these waveforms is much larger than at COR.

Strong ground motion recordings of the mainshock indicate that relatively long-period moment release began about 1 s after the onset of rupture [*Oppenheimer et al.*, 1993], consistent with the existence of a precursor similar to that shown in Figure 7. *Oppenheimer et al.* [1993] locate the rupture onset 4 km east of the source of a large-amplitude pulse of relatively long-period moment release that dominates the accelerometer recordings. This major pulse originates close to our estimate of the rupture centroid (Figure 6). *Ammon et al.* [1993] located the Cape Mendocino centroid offshore because the preliminary CALNET location used for the Honeydew event was about 5 km southwest of the final location shown in Figure 6.

Focal mechanism solutions for the Honeydew earthquake vary significantly in fault dip estimates. *Dziewonski et al.* [1992] obtain a shallow thrusting mechanism (strike/dip/rake: 311°/22°/51°) using a CMT algorithm, while the moment tensor solution given by the NEIC (48°/38°/141°) and the first motion mechanism of CALNET (308°/40°/64°) (D. Oppenheimer, personal communication, 1993) have steeper-dipping fault planes. The NEIC solution has a very similar auxillary plane to the CMT solution, and the fault strike is not well resolved. The CALNET solution is not very well

constrained, perhaps accounting for the different estimate of fault plane orientation. To investigate how these different focal mechanisms might affect the RSTFs, we calculated synthetic surface wave seismograms for the mainshock using the CMT mainshock solution and synthetics for the Honeydew event using the CMT and CALNET solutions, at azimuths that match our station distribution. We then deconvolved both sets of synthetic Honeydew waveforms from the mainshock synthetic seismograms. The resulting RSTFs for the Honeydew CMT solution were simple and stable, while the Honeydew CALNET mechanism synthetics produced unstable RSTFs for some stations, especially for Rayleigh waves. Since the observed RSTFs are simple and stable, we infer that the Honeydew and Cape Mendocino events must have had similar faulting mechanisms, as indicated by the CMT solutions.

Cape Mendocino Aftershocks

The two large strike-slip aftershocks of April 26, 1992 (M_W = 6.5, 6.6; AS 1 and 2, respectively), occurred off-shore, west of the mainshock epicenter (Figure 1) at depths near 20 km (AS 1) and 22 km (AS 2). It has been noted that the two events ruptured the mantle of the Gorda plate along different faults than the mainshock [*Oppenheimer et al.*, 1993]. These two aftershocks produced different damage patterns although they are virtually colocated and have very similar focal mechanisms and seismic moments. On the basis of seismicity, *Oppenheimer et al.* [1993] identify the southeast striking plane (Az = 132°) as the fault plane for AS 2, although the seismicity patterns are rather diffuse. They where unable to uniquely identify the fault plane for AS 1 because of the paucity of aftershocks in its vicinity, but they suggested that the northeast striking fault plane ruptured during this event. They also suggested that large, high-frequency P wave amplitude differences between AS 1 and AS 2 near azimuths of 130° are due to rupture directivity.

The EGF chosen for the analysis of these two aftershocks occurred on March 8, 1992 (M_W = 5.5), located just on-shore, approximately 25 km from the aftershock epicenters (Figure 1). This distance between the EGF and the larger events is farther than preferred; it is sufficiently close to resolve the basic character of the source functions, but estimation of any directivity effects is difficult. Since we require stations with adequate signal-to-noise ratios, the small size of the EGF limits our analysis to relatively close stations, restricting the azimuthal coverage.

The RSTFs of the larger aftershock (AS 2) contain two pulses of energy release (Figure 8) with systematic relative behavior despite a rather high noise level, which is attributable to the limited bandwidth of the EGF. More than 20 distinct phases were available for deconvolution, spanning directivity parameters from -0.25 to 0.25 s/km. We low-pass filter the RSTFs at 5 s and pick times for the onset, the first peak (peak 1), the second peak (peak 2), and the end, again noting the difficulties associated with filter sidelobes and high noise levels. Directivity analysis of the time picks between peaks 1 and 2 gives an azimuth of 148 ± 34°, with a time separation of 5.8 ± 0.6 s, a distance separation of 11.8 ± 3.4 km, and a correlation coefficient of 0.72 (Figure 8 and Table 2). Since the two distinct features in the source function can be reliably measured without bias due to filter sidelobes or dispersion effects, this type of directivity analysis should resolve a reasonable rupture velocity [e.g., *Beck and Ruff*, 1985, 1987].

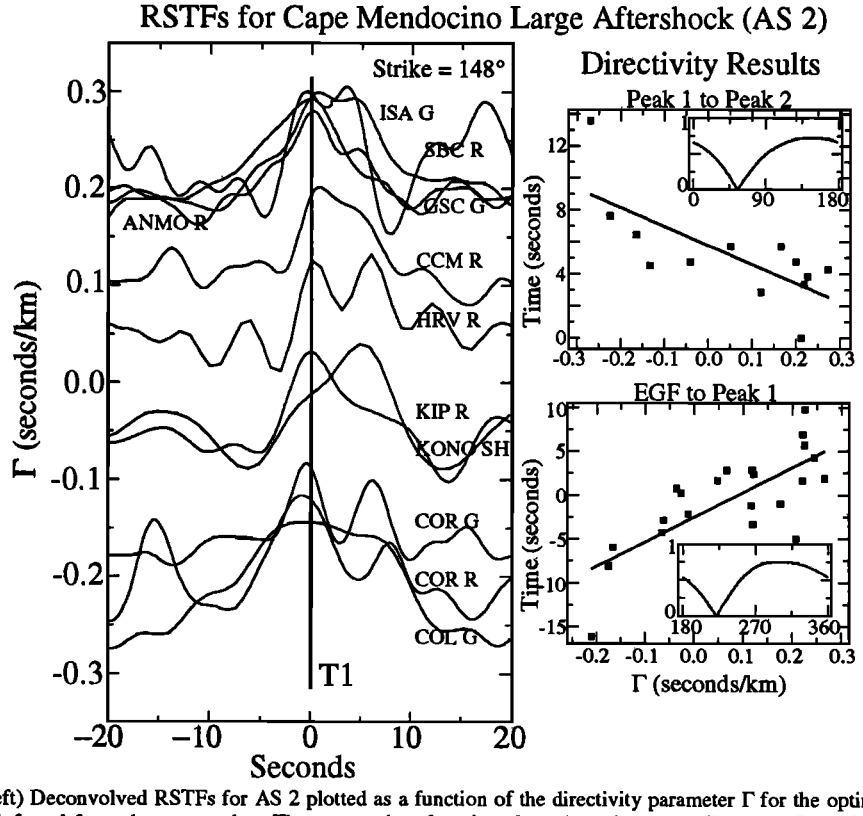

Fig. 8. (left) Deconvolved RSTFs for AS 2 plotted as a function of the directivity parameter Γ for the optimal rupture direction of 148°, inferred from the two peaks. The source time functions have been low-pass filtered at 5 s. Note the two pulses of energy release and their relative moveout as a function of directivity parameter. (right) Analysis of directivity between the time picks for the two peaks (right top) and the EGF to first peak (right bottom) as in Figure 5.

In this case, we estimate a rupture velocity of about 2 km/s, whereas the (biased) values inferred using onset or end measurements are less than 1.5 km/s.

The focal mechanism for AS 2 (Table 1) has one nodal plane striking southeast. Thus the rupture propagated on the plane striking 132°, consistent with the fault plane inferred from seismicity [*Oppenheimer et al.*, 1993]. The analysis of onset to end measurements gives an azimuth of 143 ± 35° also supporting the southeast rupture propagation. We also located these RSTF features relative to the EGF and found consistent results (Table 2). The total duration from onset to end is about 13.5 s, which is somewhat longer than the mainshock, despite the much lower moment (Table 1).

Comparison of *P* wave seismograms at different azimuths show differences in amplitudes and frequency content between the mainshock and the two aftershocks [*Oppenheimer et al.*, 1993]. *P* wave amplitudes for AS 2 are 4 times greater and contain higher frequencies that AS 1 seismograms at azimuths near 130°. *Oppenheimer et al.* [1993] attribute this difference to southeast rupture directivity for the larger aftershock. Furthermore, *P* wave seismograms for AS 2 show narrowed *P* wave pulses at stations CCM and HRV, both at eastern azimuths, in comparison to signals for AS 1 and the Cape Mendocino mainshock [see *Oppenheimer et al.*, 1993]. The *P* waves to these stations have takeoff angles around 30°, suggesting that there may have been an additional component of downward rupture in AS 2 that narrowed these pulses. Deconvolutions of the *P* waves for AS 2 at CCM and HRV show a single pulse in contrast to the two pulses or broadened pulse seen in the Rayleigh wave deconvolutions (Figure 9), further suggesting a downward component of rupture for AS 2. Our coverage is insufficient to attempt to resolve the combined horizontal and vertical directivity, but there is reasonably strong evidence that AS 2 ruptured both downward and to the southeast on a fault plane striking 132°.

RSTFs for the smaller aftershock (AS 1) show several pulses of energy release with a low-pass filter below 5 s (Figure 10). Only 17 traces yielded relatively stable deconvolutions. Identifying coherent features in these RSTFs is difficult given the noise levels and what appears to be two or possibly three interfering pulses. Instead of trying to pick these various features, we low-pass filter the RSTFs at 10 s and only pick the onset, peak, and end times of the traces in an attempt to detect any gross directivity. The directivity results for these relatively heavily filtered RSTFs are much more ambiguous for this event than for the larger aftershock. Our azimuthal coverage for this event is poor; in particular, we lack stations to the northeast. The onset-to-end analysis gives an azimuth of 87 ± 27°, a duration of 17.0 s, and a poor 0.32 correlation coefficient (Table 2). There does not appear to be a strong overall unilateral component. The onset to first peak analysis also gives a low correlation, with an azimuth of 56 ± 34°, which may be a bit more reliable given that the peak is probably less affected by the multiple subevent character. The locations relative to the EGF have high correlation coefficients (Table 2) and indicate more northerly locations relative to AS 2. Thus we cannot resolve the fault plane for this event with confidence, but what indications we find provide a weak preference for the northeast trending plane, conjugate to that which ruptured in AS 2.

We plot the (5 s filtered) RSTFs for AS 1 in Figure 10 using directivity parameters with respect to the northeast striking nodal plane (strike = 35°). There is an indication of a

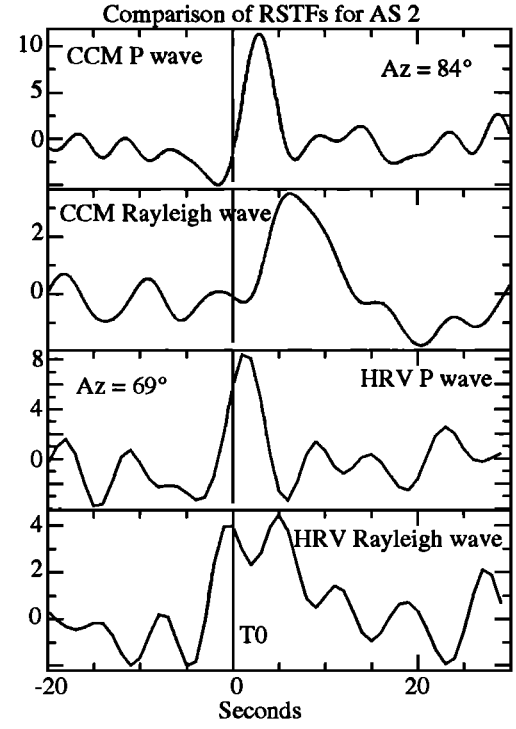

Fig. 9. *P* wave and Rayleigh wave RSTFs for AS 2 for stations CCM and HRV. The takeoff angles to stations CCM and HRV are approximately 30° and the *P* wave deconvolutions show a single main pulse of energy release while the Rayleigh wave deconvolutions show two pulses. The *P* wave deconvolutions also show higher amplitudes than the Rayleigh wave deconvolutions. The differences suggests some fast downward propagation for this event, causing constructive interference between the two pulses for the teleseismic *P* waves.

secondary pulse which moves out symmetrically with respect to $\Gamma = 0.0$ s/km, as would be expected for a bilaterally rupturing fault [e.g., *Schell and Ruff*, 1989], which may explain the poor correlations for the more heavily filtered traces when a unilateral rupture model is tested. The somewhat higher damage levels for AS 1 at northeastern azimuths, relative to those for AS 2, provides additional evidence for the northeast trending rupture plane. Thus qualitative assessment of the RSTFs for the two aftershocks indicates that AS 1 most likely ruptured the northeast trending fault plane, while AS 2 ruptured the southeast trending fault plane.

Gorda Plate Earthquakes

In analyzing the Gorda 1 and Gorda 2 events, we use EGFs from an event that occurred on August 16, 1991 (M_W = 6.2), one day before the Gorda 2 event. The NEIC locates the EGF and Gorda 1 events approximately 50 km apart, consistent with our relative location analysis, and thus this EGF is not ideal to correct for propagation effects at high frequencies. However, this is the only available event in the region large enough to be well recorded by globally distributed stations, and more than 35 phases were retrieved for analysis. The resulting RSTFs for Gorda 1 indicate a rupture with two clear pulses of moment release (Figure 11). Since the distance between the EGF and Gorda 1 is larger than 2 times the fault length, dispersion effects bias directivity analyses using onset to end time picks, which can be seen with the poor correlation coefficients in Table 2. However, moderate dispersion will not significantly affect RSTFs that show discrete subevents. The analysis for directivity between the two peaks gives a fair correlation

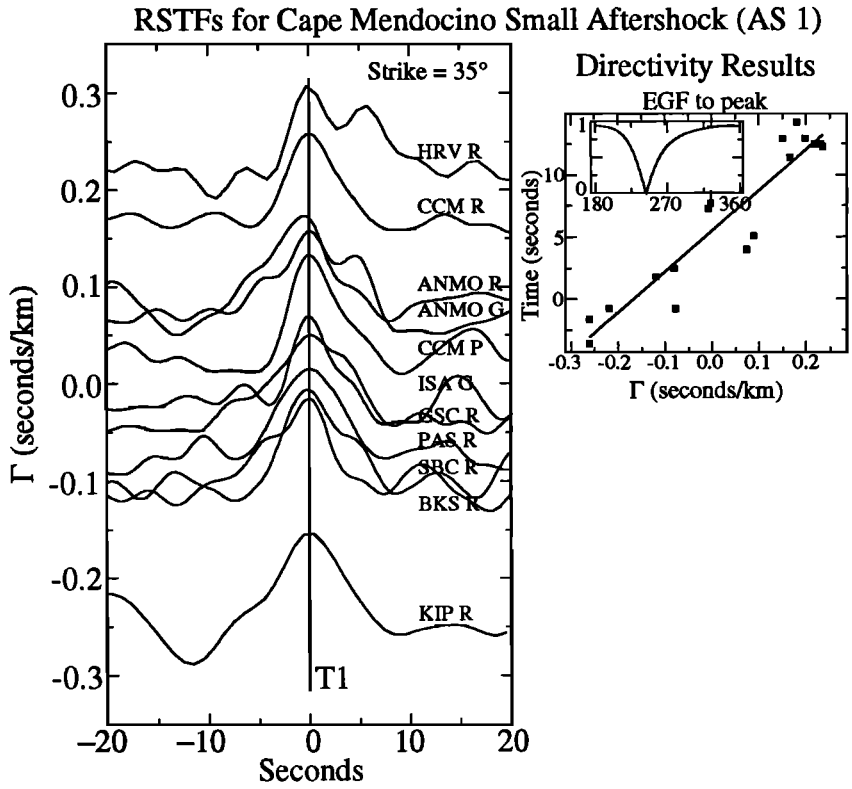

Fig. 10. (left) Deconvolved RSTFs for AS 1 plotted as a function of the directivity parameter Γ. We fix the reference rupture direction azimuth at 35°, corresponding to our preference for the choice of fault plane. The functions have been low-pass filtered at 5 s. The noisy deconvolutions and the limited directivity function coverage do not allow for reliable directivity analysis. The RSTFs show multiple pulses of energy release, with a suggestion of secondary shoulders that move out symmetrically with respect to Γ = 0.0 s/km, which may be the result of bilateral slip on this fault plane. (right) Directivity analysis for the EGF to peak (right top) relative time picks using a low-pass filter at 10 s. This places the centroid northward with respect to the EGF in comparison to AS 2, compatible with rupture on the northeast plane.

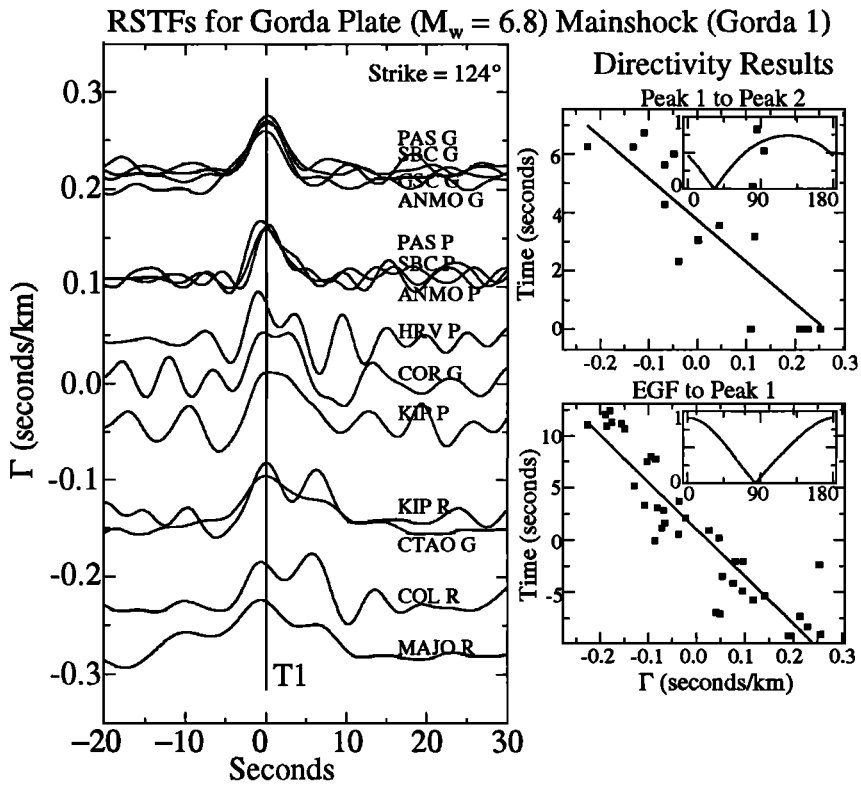

Fig. 11. (left) Deconvolved RSTFs for Gorda 1 plotted as a function of the directivity parameter Γ for the optimal rupture azimuth of 124°. The functions have been low-pass filtered at 5 s. Note the two pulses of energy release, which converge for positive Γ and separate for negative Γ. (right) Analysis of directivity between the time picks for the two peaks (right top) and for the EGF to peak (right bottom).

coefficient (0.60) indicating southeastward rupture propagation along an azimuth of 120° (Figure 11 and Table 2), conjugate to the rupture direction of the northeast trending 1980 Eureka event. The directivity effects on the RSTFs are illustrated in Figure 11 by the merging of the two pulses into one pulse with increasing Γ. While it is possible that rupture occurred on two offset northeast trending faults, the simpler interpretation is that rupture occurred on the nodal plane striking 315° (Table 1), with some unilateral propagation toward the southeast and involving two subevents. The relative location of the EGF with respect to the onset of moment release is similar to the NEIC location, with the distance between the two events being approximately 45 km.

The Gorda 2 RSTFs are very stable and show a smooth rupture with a short duration (Figure 12). In this case the EGF is within 15 km of the rupture, so it is highly suitable for correcting the propagation effects, and there are about 28 phases that provide good sampling of the directivity function. The magnitude of any unilateral directivity is small and difficult to resolve. Using onset to end time picks, we find the rupture propagated to the southwest, indicating a southwest-northeast oriented fault plane. This fault orientation coincides with the fabric of the northeast striking structures mapped within the plate. The average duration is around 7 s, very short to resolve significant directivity using a low-pass filter of 5 s, and the magnitude of the directivity is only a few seconds (Figure 12). However, even with such a short duration, the subtle directivity information indicates a southwest propagating rupture. Locating the onset, peak and end relative to the EGF confirms the southwestward direction of rupture (Table 2). Thus the two Gorda plate earthquakes ruptured southeast and southwest striking fault planes, indicating that conjugate faulting occurs in the central Gorda plate as well as at the MTJ.

DISCUSSION

This analysis of relative source time functions (RSTFs) obtained by empirical Green function (EGF) deconvolution has allowed us to identify the fault rupture planes, to determine the rupture durations, and to characterize rupture complexities for the Cape Mendocino earthquake, its two largest aftershocks, and the two large Gorda plate events. The variable fault orientations and rupture complexities indicate a complicated deformation regime near the MTJ.

Fault Orientations

We summarize our results on fault plane and rupture direction determination from seismic wave directivity in Figure 13. The arrow next to each focal mechanism in Figure 13 points to the preferred fault plane as well as indicating the direction of any unilateral component of rupture propagation. This extent of faulting information, particularly for modest-sized earthquakes located offshore, has not been widely available in the past, given the limitations of most forward modeling procedures. Inclusion of broadband surface waves to extend the sampled range of the directivity function was critical to identifying these faults. At present, high-resolution time functions for surface waves can only be reliably isolated using the empirical Green function approach.

A shallow dipping thrust plane ruptured during the Cape Mendocino event, and the centroid of moment release was centered just onshore. The rupture propagated updip and

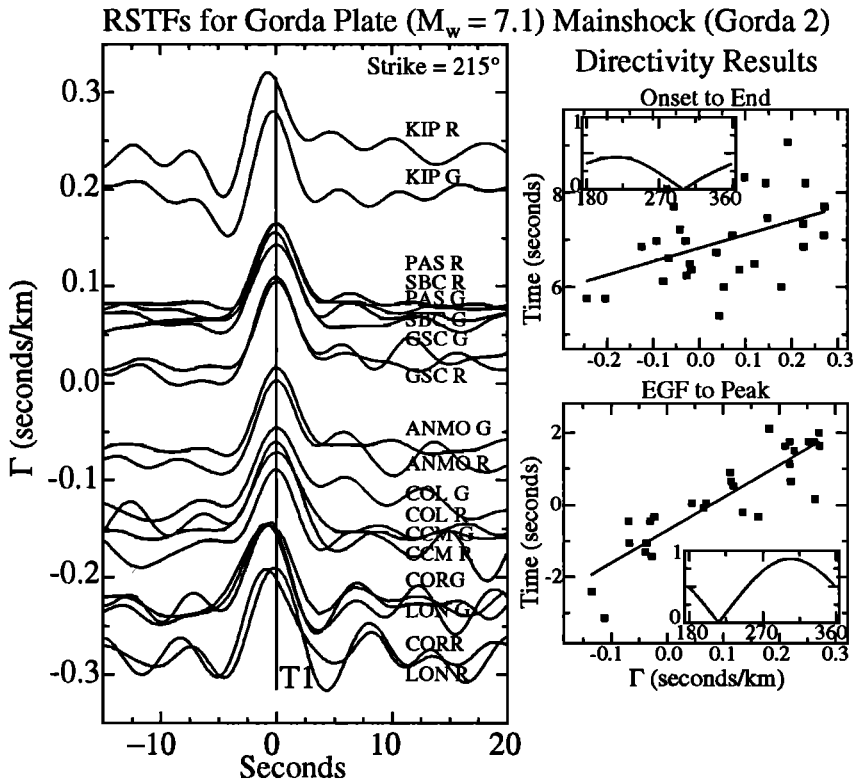

Fig. 12. (left) Deconvolved RSTFs for Gorda 2 plotted as a function of the directivity parameter Γ for the optimal rupture direction of 215°. The functions have been low-pass filtered at 10 s. Note the short duration and smooth rupture. This event shows only very subtle directivity. (right) Directivity analysis for onset to end (right top) and EGF to peak (right bottom) time picks.

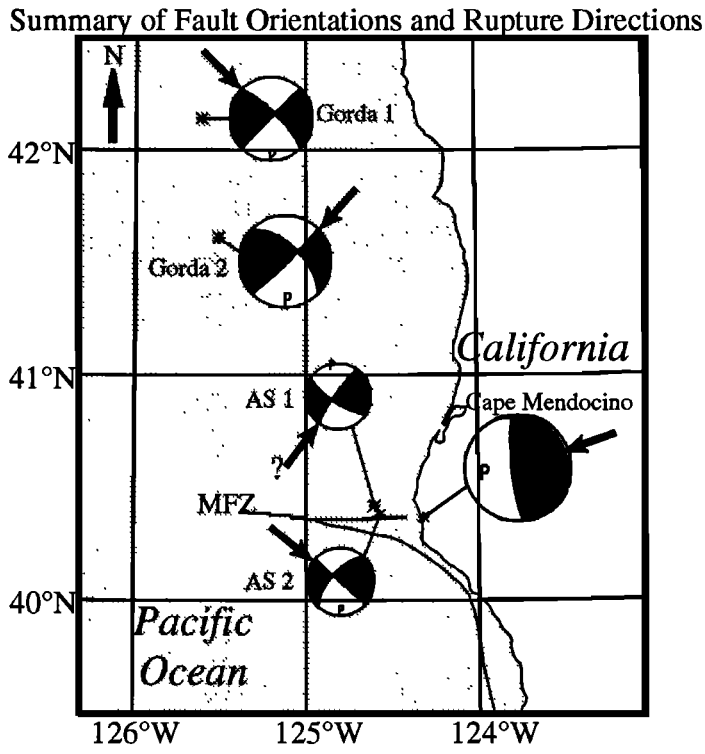

Fig. 13. Summary of fault orientations and rupture directions for the Cape Mendocino mainshock, its aftershocks, and the Gorda plate events. Each focal mechanism is labeled by an arrow which points to the rupture plane in the rupture direction.

appears to have had a small precursory phase of weak radiation in the first second of the event. The location of the primary moment release is generally consistent with the aftershock distribution, which is also concentrated near the coast; however, very few aftershocks are known to have thrust mechanisms, so any relationship to the aftershocks is ambiguous, and no clear planar structure is apparent in the seismicity [*Oppenheimer et al.*, 1993]. The slip direction obtained from preliminary geodetic modeling is also generally consistent with our inferred rupture direction [*Oppenheimer et al.*, 1993]. We suspect, but cannot demonstrate, that the Honeydew earthquake, with its close proximity and similar focal mechanism, most likely ruptured the same fault plane as the Cape Mendocino mainshock. *McPherson and Dengler* [1991] invoke geological data to suggest that the Honeydew earthquake ruptured the southwestward dipping fault plane, but we were unable to find a suitable EGF to independently test their interpretation.

The mainshock fault orientation is consistent with Gorda plate-North American plate convergence and thus it may be the first large earthquake to be recorded in the Cascadia subduction zone [*Michael*, 1992; *Oppenheimer et al.*, 1993]. However, seismic structural studies within the region demonstrate that the onshore extension of the Gorda plate is deeper (~20 km) than the reported depth (< 15 km) of the mainshock (D. Verdonck and G. Zandt, 1993). The event may have ruptured a fault parallel or subparallel to the main interplate contact. The existence of a double seismic zone identified by relocation of earthquakes [*Smith et al.*, 1993] supports the hypothesis that this earthquake ruptured within the North American plate, or at least in a complex interplate shear zone. Eastward migration of the San Andreas has been suggested as the cause of this parallel fault [*Smith et al.*, 1993]. Since the mainshock may be an intraplate event that occurred in this complex tectonic region, it is difficult to assess the effect on the seismic potential for the Cascadia subduction zone to the north.

The two large strike-slip Cape Mendocino aftershocks ruptured the mantle of the Gorda plate [*Oppenheimer et al.*, 1993] and were triggered by the mainshock. Our results suggest that these earthquakes ruptured conjugate planes (Figure 13). The larger aftershock (AS 2) shows southeast and downward directivity, which is most likely responsible for the event being felt as far south as Santa Cruz and Salinas. The directivity of the smaller aftershock is much more subtle but appears to have ruptured on the northeast trending fault, with weak unilateral and perhaps bilateral faulting. The differences in shaking and regional damage between the two aftershocks from preliminary intensity maps of the region [*Dengler et al.*, 1992a] can be explained by rupture on conjugate fault planes. North-south compression between the Gorda and Pacific plates appears to be responsible for the ongoing deformation of the southern Gorda plate [*Silver*, 1971; *Stoddard*, 1987]. Thus the conjugate-faulting aftershocks are primarily the result of Gorda-Pacific plate interaction rather than the Gorda-North American plate motion that produced the mainshock. However, static stress modeling indicates that the offshore events may have been triggered by the small stress perturbations associated with the Cape Mendocino mainshock [*Oppenheimer et al.*, 1993].

The Gorda plate events occurred on northwest-southeast (Gorda 1) and northeast-southwest (Gorda 2) fault planes. The Gorda 1 fault plane orientation is not consistent with the primary structural orientations in the Gorda plate mapped by *Silver* [1971] (Figure 13), but both of these earthquakes also relieve the north-south compression within the plate. This sequence of events, including the August 16, 1991, EGF is a further illustration of the complex deformation within the Gorda plate. It is unclear whether this intraplate

accommodation of north-south compression affects the seismic potential of the Cascadia subduction zone.

Rupture Complexities

The variation in duration and seismic moment between the events analyzed here suggest significant differences in the nature of these ruptures. In order to investigate this further, we stack the RSTFs for each event to improve the signal to noise ratio and to suppress any bias due to radiation pattern differences between the mainshock and EGF. The traces are aligned on the main peak and then summed. This procedure smoothes the minor directivity effects, and we omit the RSTFs with large values of Γ, to ensure that the stacks emphasize the azimuthally common features. The resulting stacked RSTFs for all five events studied show good resolution and high signal-to-noise ratios (Figure 14). In each case the filter corner is 5 s, so an impulse would have a 5-s duration, and any shorter-period features have been lost by the filtering and stacking. The Cape Mendocino mainshock and Gorda 2 both have a single pulse of energy release, while AS 1, AS 2, and Gorda 1 have at least two pulses of energy release. We also create synthetic source time functions by fitting filtered triangular functions that closely match the RSTFs (Figure 14). The total pulse durations from the stacked RSTFs are 9 s for the Cape Mendocino mainshock, 15 s for AS 1, 14 s for AS 2, 10 s for Gorda 1, and 8 s for Gorda 2 (Table 3). The synthetic source time functions give similar durations (Figure 4) that should not be biased by the 5-s filter. The relatively long duration of the two aftershocks and their

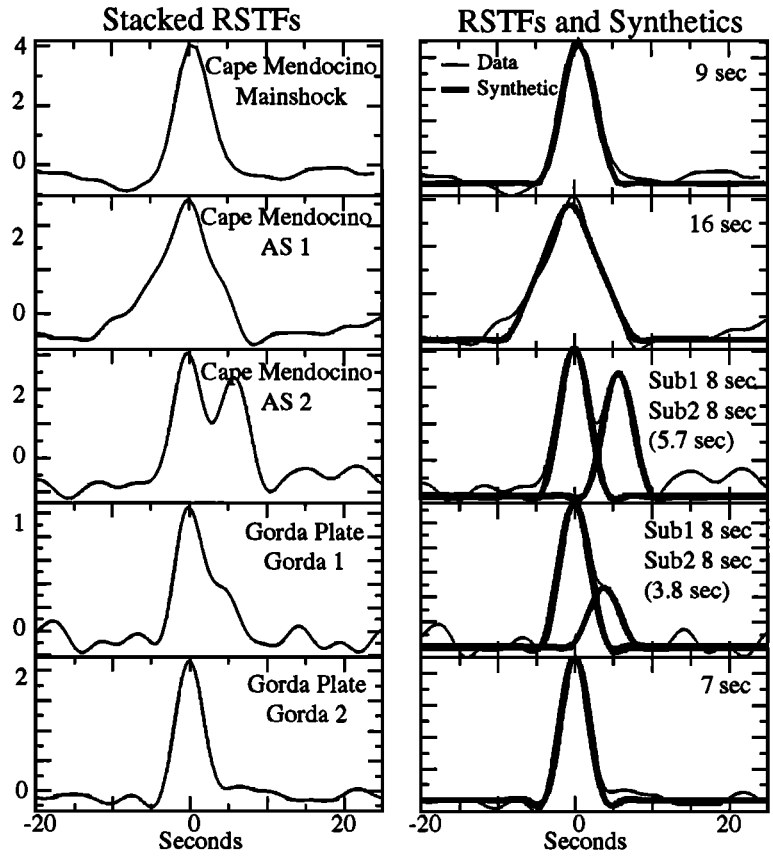

Fig. 14. (left) Stacked RSTFs for the Cape Mendocino mainshock, its two large aftershocks, and the two large Gorda plate events. The RSTFs for each event were aligned on the peak of moment release and stacked, after removing stations with significant directivity (large Γ values). While there is some averaging due to finiteness effects, these represent the basic time histories of each rupture. Note the multiple pulses of energy release and long durations for the two aftershocks. (right) Synthetic and stacked source time functions for each event. The synthetic time functions were created using filtered (5 s low pass) triangular functions with the total duration labeled for each earthquake. For earthquakes with subevents, the number in parentheses signifies the time separation between subevents.

TABLE 3. Stress Drops and Moment Ratios

Event	Duration, s	Δσ(A4),* MPa	Δσ(3.0),+ MPa	Δσ(2.5),+ MPa	Δσ(2.0),+ MPa	M_o‡ / M_o^{EGF}	M_o§ / M_o^{EGF}
CM	9.2	0.89	1.35	2.31	4.55	32.4	35.2
AS1	15.0	0.02	0.07	0.11	0.22	21.3	32.2
AS2	14.0	0.06	0.09	0.16	0.31	34.7	53.9
Gorda 1	10.4	0.77	0.30	0.52	1.02	6.0	6.6
Gorda 2	7.8	1.50	1.51	2.61	5.11	14.3	14.1

* From equation (A4).
+ From equation (A5) assuming rupture velocity (in parentheses).
‡ From stacked RSTF.
§ From CMT catalogue.

complexity of energy release perhaps suggest a difference in the nature of earthquake faulting occurring in the mantle versus the crust. One method to quantify this difference is by calculation of the associated stress drops.

We calculate stress drop using the methods of *Houston* [1990] and *Kanamori and Anderson* [1975] (see the appendix). We assume that the stacked RSTFs are the actual azimuthally averaged moment rate function scaled by the moment of the EGF (Figure 14). Since we low-pass filter either at 5 or 10 s, the stress drops that we obtain from the RSTFs will be low-frequency stress drops. We also assume that the corner frequencies for the mainshocks are contained within our bandwidth, which may not hold for the smaller subevents in the aftershocks. We compare the moment ratios of the events and EGFs predicted by the CMT solutions to those obtained by integrating the RSTFs (Table 3) to check whether we are obtaining the total moment from the stacked RSTFs. We find excellent agreement between the stacked RSTFs and the CMT catalog moments, except for the two aftershocks. The moment ratios for both aftershocks are approximately 40% lower than the CMT solutions predict. Since both earthquakes show this behavior, it is possible that the reported CMT moment for the EGF is too low. Alternatively, since we do not have excellent azimuthal coverage for these smaller events, it is possible that the stacked RSTFs still contain minor effects of focal mechanism differences between the mainshocks and EGF.

Table 3 lists dynamic and static stress drop estimates obtained from the scaled RSTFs. For the static stress drop calculations, we assume various rupture velocities in mapping the total pulse duration to a circular fault radius. The Orowan stress drop equation given by (A4) requires P wave and S wave velocities, density, and shear modulus. We use the crustal values in Table 4 for the Cape Mendocino mainshock and the Gorda events and the mantle values for the aftershocks. The stress drop estimates obtained from the RSTFs should be considered a lower bound of stress drop since the total duration includes the rise time, duration, and the fall time. The average dynamic stress drops are 0.9 MPa for the Cape Mendocino mainshock, 0.02 MPa for AS 1, 0.06 MPa for AS 2, 0.8 MPa for Gorda 1, and 1.5 MPa for Gorda 2. The static stress drops for rupture velocities near 3.0 km/s are comparable, while higher values are found for slower rupture velocities. We also estimate the upper bound of static stress drop by using the half duration (risetime) of the synthetic source time functions (Table 5). These results are significantly higher, as expected. However, regardless of the chosen technique, it appears that the two aftershocks had a significantly lower overall stress drop than the other events. Since the RSTFs for the aftershocks are stacked and low-pass filtered at 5 s, we do not see any differences in the high-frequency content in the P waves for AS 2 relative to AS 1. If there is significant high-frequency energy release for these events [*Oppenheimer et al.*, 1993], our stress drop calculations are probably biased low. If we calculate stress drop for the two pulses of AS 2 separately, the stress drops increase dramatically (Table 5) but are not greater than the other crustal events. The stacked functions do provide the gross characteristics of these two ruptures, and the relative stress drops appear robust to first order. It thus appears that the intraplate events rupturing in the mantle have a somewhat lower stress drop and more complex faulting than the crustal events. Establishing whether this relationship holds for other regions is important.

TABLE 4. Crustal Model Parameters

Parameter	Crust	Mantle
P velocity, km/s	6.0	8.0
S velocity, km/s	3.5	4.5
Density, kg/m^3	2.7×10^3	3.3×10^3
Rigidity, MPa	3.2×10^4	6.7×10^4

CONCLUSION

We apply the empirical Green function method to large data sets of both body and surface waves to obtain broadband source time functions for recent events in the vicinity of the Mendocino Triple Junction and the Gorda plate. We find that we can extend the method to smaller magnitude earthquakes than previously considered, retrieving basic information about the fault orientation and rupture complexity for offshore events larger than M_W = 6.5. Directivity results show that the Cape Mendocino mainshock ruptured a shallow dipping plane with a duration of 9 s and a dynamic stress drop of 0.9 MPa. The two large aftershocks of this event occurred in the mantle on conjugate strike-slip faults and had more complicated ruptures with multiple pulses of energy release, longer durations, and stress drops less than 0.3 MPa. The Gorda plate events ruptured both southwest and southeast striking faults, highlighting the complex deformation within the Gorda plate caused by north-south compression. These events had moderate stress drops and durations of less than 11 s.

APPENDIX

Stress drop is calculated by first stacking the RSTFs for each event to improve the signal-to-noise ratio and to reduce any bias in the source time functions due to mechanism differences between the EGF and mainshock. We assume that the stacked RSTFs are the moment rate function scaled by the moment of the EGF. In this case, the moment rate function is

$$\dot{M}(t) = M_o^{\mathrm{EGF}} R(t), \tag{A1}$$

where M_o^{EGF} is the moment of the EGF and R(t) is the stacked RSTF. The Orowan stress drop presented by *Houston* [1990], which is the average dynamic stress drop that depends on the energy of the rupture process, is given by

$$\Delta\sigma = \frac{2uE_s}{M_o^{\mathrm{Main}}}, \tag{A2}$$

TABLE 5. Upper Bounds of Static Stress Drops From Synthetic Source Time Histories

Event	Duration, s	$\Delta\sigma(3.0)$,* MPa	$\Delta\sigma(2.5)$,* MPa	$\Delta\sigma(2.0)$,* MPa	Moment %
CM	4.5	11.00	20.50	40.10	100
AS1	8.0	0.19	0.33	0.64	100
AS2	9.7	0.17	0.30	0.59	100
Sub1	4.0	1.36	2.35	4.60	55
Sub2	4.0	1.11	1.93	3.76	45
Gorda 1	7.8	0.70	1.21	2.37	100
Sub1	4.0	3.65	6.31	12.32	70
Sub2	4.0	1.56	2.70	5.28	30
Gorda 2	7.0	16.70	28.90	56.50	100

*From equation (A5) assuming rupture velocity (in parentheses).

where

$$E_s = \frac{1}{5\pi\rho}\left[\frac{1}{3\alpha^5}+\frac{1}{2\beta^5}\right]\int_{-\infty}^{\infty}\ddot{M}^2(t)\,dt. \quad \text{(A3)}$$

M_o^{Main} is the moment of the mainshock, μ the shear modulus, E_S is the seismic energy, ρ the density, α is the seismic P wave velocity, and β is the seismic S wave velocity. Substituting (A1) and (A3) into (A2), we find that the Orowan stress drop equals:

$$\Delta\sigma = \frac{1}{5\pi\rho}\left[\frac{1}{3\alpha^5}+\frac{1}{2\beta^5}\right]\frac{M_o^{\text{EGF2}}}{M_o^{\text{Main}}}\int_{-\infty}^{\infty}\dot{R}^2(t)\,dt. \quad \text{(A4)}$$

Thus, assuming values for density, velocity, and the shear modulus (Table 4), we can easily compute stress drop from our stacked RSTFs.

The static stress drop derivation is given by *Kanamori and Anderson* [1975]. For a circular fault, they define stress drop as

$$\Delta\sigma = \frac{7}{16}\frac{M_o}{a^3}, \quad \text{(A5)}$$

where a is the radius of the fault. a can be assumed to be the rupture velocity times the duration of rupture. Assuming a rupture velocity, we compute a using the duration of rupture from the stacked RSTF and obtain the static stress drop.

Acknowledgments. We thank the IRIS Data Management Center for its open access to global digital data. Aaron A. Velasco was supported by a dissertation year fellowship from the Ford Foundation. We thank Paul Spudich, George Zandt, and an anonymous reviewer for constructive comments on the manuscript. This research was supported by NSF grant EAR-9017767 with facilities support provided by the W. M. Keck Foundation. Contribution 210 of the Institute of Tectonics and C. F. Richter Seismological Laboratory.

REFERENCES

Ammon, C. J., A. A. Velasco, and T. Lay, Rapid estimation of rupture directivity: Application to the 1992 Landers (M_S = 7.4) and Cape Mendocino (M_S = 7.2) California earthquakes, *Geophys. Res. Lett., 20*, 97-100, 1993.

Atwater, B., Evidence for great Holocene earthquakes along the outer coast of Washington state, *Science, 236*, 942-944, 1987.

Atwater, T., Implications of plate tectonics for the Cenozoic tectonic evolution of western North America, *Geol. Soc. Am. Bull., 81*, 3513-3536, 1970.

Beck, S., and L. Ruff, The rupture process of the 1976 Mindanao earthquake, *J. Geophys. Res., 90*, 6773-6782, 1985.

Beck, S. L., and L. J. Ruff, Rupture process of the great 1963 Kurile Islands earthquake sequence: Asperity interaction and multiple event rupture, *J. Geophys. Res., 92*, 14,123-14,138, 1987.

Bolt, B. A., C. Lomnitz, and T. V. McEvilly, Seismological evidence on the tectonics of central and northern California and the Mendocino escarpment, *Bull. Seismol. Soc. Am., 58*, 1725-1767, 1968.

Christensen, D. H., and L. J. Ruff, Analysis of the trade-offs between hypocentral depth and source time function, *Bull. Seismol. Soc. Am., 75*, 1637-1656, 1985.

Clarke, S. H., Jr., and G. A. Carver, Late Holocene tectonics and paleoseismicity, southern Cascadia subduction zone, *Science, 255*, 188-192, 1991.

Clayton, R. W., and R. A. Wiggins, Source shape estimation and deconvolution of teleseismic body waves, *Geophys. J. R. Astron. Soc., 47*, 151-177, 1976.

Cockerham, R.S., Evidence for a 180 km long subducted slab beneath northern California, *Bull. Seismol. Soc. Am., 74*, 569-576, 1984.

Dengler, L., K. Moley, A. Lehre, and D. Materson, Isoseismal maps of the April 25-26, 1992 Cape Mendocino earthquake sequence, *Eos Trans. AGU, 73 (43)*, Fall Meeting suppl., 503, 1992a.

Dengler, L. A., G. Carver, and R. McPherson, Sources of North Coast seismicity, *Calif. Geol., 45*, 40-53, 1992b.

Dickinson, W. R., and W. S. Snyder, Geometry of the triple junctions related to San Andreas Transform, *J. Geophys. Res., 84*, 561-572, 1979.

Dziewonski, A. M., and D. L. Anderson, Preliminary reference Earth model, *Phys. Earth Planet. Inter., 25*, 297-356, 1981.

Dziewonski, A. M., G. Ekström, and M P. Salganik, Centroid-moment tensor solutions for July-September 1991, *Phys. Earth Planet. Inter., 72*, 1-11, 1992.

Dziewonski, A. M., G. Ekström, and M. P. Salganik, Centroid-moment tensor solutions for January-March, 1992, *Phys. Earth. Planet Inter., 77*, 143-150, 1993a.

Dziewonski, A. M., G. Ekström, and M. P. Salganik, Centroid-moment tensor solutions for April-June, 1992, *Phys. Earth. Planet Inter., 77*, 151-163,1993b.

Ekström, G., R. S. Stein, J. P. Eaton, and D. Eberhart-Phillips, Seismicity and geometry of a 110-km-long blind thrust fault, 1, The 1985 Kettleman Hills, California, earthquake, *J. Geophys. Res., 97*, 4843-4864, 1992.

Ellsworth, W. L., Earthquake history, 1769-1989, The San Andreas fault system, California, *U.S. Geol. Surv. Prof. Pap. 1515*, 153-181, 1990.

Furlong, K. P., W. D. Hugo, and G. Zandt, Geometry and evolution of the San Andreas fault zone in northern California, *J. Geophys. Res., 94*, 3100-3110, 1989.

Gee, L. S., R. A. Urhammer and B. Romanowicz, Source parameters and rupture characteristics of the Gorda Basin earthquakes and their tectonic implications, *Eos Trans. AGU, 72 (44)*, Fall Meeting suppl., 312, 1991.

Griscom, A., and R. C. Jachens, Tectonic history of the north portion of the San Andreas fault system, California, inferred from gravity and magnetic anomalies, *J. Geophys. Res., 94*, 3089-3099, 1989.

Hartzell, S., Earthquake aftershocks as Green's functions, *Geophys. Res. Lett., 5*, 1-5, 1978.

Heaton, T. H., and S. H. Hartzell, Earthquake hazards on the Cascadia subduction zone, *Science, 236*, 162-168, 1987.

Heaton, T.H., and H. Kanamori, Seismic potential associated with subduction in the northwestern United States, *Bull. Seismol. Soc. Am., 74*, 933-941, 1984.

Helmberger, D., and R. A. Wiggins, Upper mantle structure of the mid-western United States, *J. Geophys. Res., 76*, 3229-3245, 1971.

Herrmann, R. B., *Computer Programs in Seismology*, St. Louis Univ., 1987.

Hirasawa, T., Source mechanism of the Niigata earthquake of June 16, 1964, as derived from body waves, *J. Phys. Earth, 13*, 35-66, 1965.

Hough, S. E., L. Seeber, A. Lerner-Lam, and J. G. Armbruster, Empirical Green's function analysis of Loma Prieta aftershocks, *Bull. Seismol. Soc. Am., 81*, 1737-1753, 1991.

Houston, H., Broadband source spectrum, seismic energy, and stress drop of the 1989 Macquarie Ridge earthquake, *Geophys. Res. Lett., 17*, 1021-1024, 1990.

Jachens, R.C., and A. Griscom, Three-dimensional geometry of the Gorda plate beneath northern California, *J. Geophys. Res., 88*, 9375-9392, 1983.

Kanamori, H., , and D. L. Anderson, Theoretical basis of some empirical relations in seismology, *Bull. Seismol. Soc. Am., 65*, 1073-1095, 1975.

Kelsey, H.M., and G.A. Carver, Late Neogene and Quaternary tectonics associated with the northward growth of the San Andreas fault, northern California, *J. Geophys. Res., 93*, 4797-4819, 1988.

Kikuchi, M., and H. Kanamori, Inversion of complex body waves, *Bull. Seismol. Soc. Am., 72*, 491-506, 1982.

Kikuchi, M., and H. Kanamori, Inversion of complex body waves, II, *Phys. Earth Planet Inter., 43*, 205-222, 1986.

Kikuchi, M., and H. Kanamori, Inversion of complex body wave, III, *Bull. Seismol. Soc. Am., 81*, 2335-2350, 1991.

Langston, C. A., Source inversion of seismic waveforms: The Koyna, India, Earthquakes of 13 September, 1967, *Bull. Seismol. Soc. Am., 71*, 1-24, 1981.

Lay, T., J. W. Given, and H. Kanamori, Long-period mechanism of the 8 November 1980 Eureka, California, earthquake, *Bull. Seismol. Soc. Am., 72*, 439-456, 1982.

McCroy, P. A., Late Neogene geohistory analysis of the Humboldt Basin and its relationship to convergence of the Juan de Fuca plate, *J. Geophys. Res., 94*, 3126-3138, 1989.

McPherson, R.C., and L.A. Dengler, The Honeydew earthquake, *Calif. Geol., 45*, 31-39, 1991.

Michael, A., Three's a crown in California, *Nature, 357*, 111-112, 1992.

Mueller, C. S., Source pulse enhancement by deconvolution of an empirical Green's function, *Geophys. Res. Lett., 12*, 33-36, 1985.

Muhs, D. R., H. M. Kelsey, G. H. Miller, G. L. Kennedy, J. F. Whelan, and G. W. McInelly, Age estimate and uplift rates for late Pleistocene marine terraces: Southern Oregon portion of the Cascadia forearc, *J. Geophys. Res, 95*, 6685-6698, 1990.

Nakanishi, I., Source process of the 1989 Sanriku-Oki earthquake, Japan: Source function determined using empirical Green function, *J. Phys. Earth, 39*, 661-667, 1991.

National Earthquake Information Center (NEIC), Monthly listings, U.S. Geol. Surv., Denver, Co., April 1992.

Oppenheimer, D., et al., The Cape Mendocino, California earthquake sequence of April, 1992: Subduction at the triple junction, *Science, 261*, 433-438, 1993.

Riddihough, R., Recent movements of the Juan de Fuca plate system, *J. Geophys. Res., 89*, 6980-6994, 1984.

Ruff, L., Tomographic imaging of seismic sources, in *Seismic Tomography*, edited by G. Nolet, pp. 339-366, D. Reidel, Norwell, Mass., 1987.

Ruff, L., and H. Kanamori, The rupture process and asperity distribution of three great earthquakes from long-period diffracted P-waves, *Phys. Earth Planet. Inter., 31*, 202-230, 1983.

Savage, J. C., and M. Lisowski, Strain measurements and the potential for a great subduction earthquake off the coast of Washington, *Science, 252*, 101-103, 1991.

Schell, M. M., and L. J. Ruff, Rupture of a seismic gap in southeastern Alaska: The 1972 Sitka earthquake (M_S 7.6), *Phys. Earth. Planet. Inter., 54*, 241-257, 1989.

Schwartz, S. Y., Earthquake mobilization plan tested, *EOS, Trans. AGU, 71*, 277-278, 1992.

Schwartz, S. Y., and L. J. Ruff, The 1968 Tokachi-Oki and the 1969 Kurile Islands earthquakes: Variability in the rupture process, *J. Geophys. Res., 90*, 8613-8626, 1985.

Silver, E. A., Tectonics of the Mendocino triple junction, *Geol. Soc. Am. Bull., 82*, 2965-2978, 1971.

Simila, G. W., Seismological evidence on the tectonics of the northern section of the San Andreas fault region, Studies of the San Andreas fault zone in northern California, edited by R. Streitz and R. Sherburne, *Spec. Rep. Calif. Div. Mines Geol., 140*, 131-137, 1980.

Simila, G. W., W. A. Peppin, and T. V. McEvilly, Seismotectonics of the Cape Mendocino, California, area, *Geol. Soc. Am. Bull., 86*, 1399-1406, 1975.

Smith, S. W., R. C. McPherson, and N. I. Severy, The Eureka earthquake of 1980, breakup of the Gorda plate (abstract), *Earthquake Notes, 52*, 42, 1981.

Smith, S. W., J. S. Knapp, and R. McPherson, Seismicity of the Gorda plate, structure of the continental margin, and an eastward jump of the Mendocino triple junction, *J. Geophys. Res., 98*, 8153-8171, 1993.

Spence, W., Stress origins and earthquakes potentials in Cascadia, *J. Geophys. Res., 94*, 3076-3088, 1989.

Stein, R. S., and G. Ekström, Seismicity and geometry of a 110-km-long blind thrust fault, 2, Synthesis of the 1982-1985 California earthquake sequence, *J. Geophys. Res., 97*, 4865-4883, 1992.

Stoddard, P. R., A kinematic model for the evolution of the Gorda plate, *J. Geophys. Res., 92*, 11,524-11,532, 1987.

Stoddard, P. R. and M. T. Woods, Master event relocations of Gorda block earthquakes: Implications for deformation, *Geophys. Res. Lett., 17*, 961-964, 1990.

Sverdrup, K. A., Multiple-event relocation of earthquakes near the Gorda rise - Mendocino fracture zone intersection, *Geophys. Res. Lett., 14*, 347-350, 1987.

Turcotte, T., P. Somerville, and F. H. Swan, Evaluation of the seismicity data associated with the November 1980 Trinidad offshore earthquake for the Humboldt Bay power plant unit No. 3, 53 pp., Woodward-Clyde Consultants, San Fransisco, 1982.

Velasco, A. A., T. Lay, and J. Zhang, Improved resolution of earthquake source parameters from long-period surface wave inversions, *Phys. Earth Planet. Inter., 74*, 101-107, 1992.

Wilson, D.S., A kinematic model for the Gorda deformation zone as a diffuse southern boundary of the Juan de Fuca plate, *J. Geophys. Res., 91*, 10,259-10,269, 1986.

Wilson, D. S., Deformation of the so-called Gorda plate, *J. Geophys. Res., 94*, 3065-3075, 1989.

C. J. Ammon and T. Lay, Earth Science Board, Applied Science Bldg., University of California, Santa Cruz, CA, 95064

A. A. Velasco, Lawrence Livermore National Laboratory, P.O. Box 808, L-202, Livermore, CA 94551

(Received April 14, 1993;
revised August 5, 1993;
accepted August 13, 1993.)